

MAGII-CAT VI. THE Mg II INTRAGROUP MEDIUM IS KINEMATICALLY COMPLEX

NIKOLE M. NIELSEN¹, GLENN G. KACPRZAK¹, STEPHANIE K. POINTON¹, CHRISTOPHER W. CHURCHILL²,
AND MICHAEL T. MURPHY¹

¹ Centre for Astrophysics and Supercomputing, Swinburne University of Technology, Hawthorn, Victoria 3122, Australia; nikolenielsen@swin.edu.au

² Department of Astronomy, New Mexico State University, Las Cruces, NM 88003, USA

ApJ accepted 31 October 2018

ABSTRACT

By comparing Mg II absorption in the circumgalactic medium (CGM) of group environments to isolated galaxies, we investigated the impact of environment on the CGM. A Mg II absorber is associated with a group if there are two or more galaxies at the absorption redshift within a projected distance of $D = 200$ kpc from a background quasar and a line-of-sight velocity separation of 500 km s^{-1} . We compiled a sample of 29 group environments consisting of 74 galaxies (2–5 galaxies per group) at $0.113 < z_{\text{gal}} < 0.888$. The group absorber median equivalent width ($\langle W_r(2796) \rangle = 0.65 \pm 0.13 \text{ \AA}$) and covering fraction ($f_c = 0.89^{+0.05}_{-0.09}$) are larger than isolated absorbers (1.27σ and 2.2σ , respectively) but median column densities are statistically consistent. A pixel-velocity two-point correlation function analysis shows that group environment kinematics are statistically comparable to isolated environments (0.8σ), but with more power for high velocity dispersions similar to outflow kinematics. Group absorbers display more optical depth at larger velocities. A superposition model in which multiple galaxies contribute to the observed gas matches larger equivalent width group absorbers, but overpredicts the kinematics significantly due to large velocity separations between member galaxies. Finally, galaxy–galaxy groups (similar member galaxy luminosities) may have larger absorber median equivalent widths (1.7σ) and velocity dispersions (2.5σ) than galaxy–dwarf groups (disparate luminosities). We suggest the observed gas is coupled to the group rather than individual galaxies, forming an intragroup medium. Gas may be deposited into this medium by multiple galaxies via outflowing winds undergoing an intergalactic transfer between member galaxies or from tidal stripping of interacting members.

Keywords: galaxies: halos — quasars: absorption lines — galaxies: groups: general

1. INTRODUCTION

Extensive work has gone into investigating the role that the baryon cycle plays in forming galaxies and steering their evolution, with particular focus on gas reservoirs such as the circumgalactic medium (CGM). It is well-known that the baryon cycle regulates star formation in galaxies via a balance of inflowing and outflowing gas (e.g., Oppenheimer & Davé 2008; Lilly et al. 2013), processes which must take place in and contribute material to the CGM of galaxies. The build-up of material into the CGM results in a gas reservoir with a mass comparable to the interstellar medium (Thom et al. 2011; Tumlinson et al. 2011; Werk et al. 2013; Peebles et al. 2014) out to large distances ($D \gtrsim 150$ kpc; e.g., Chen et al. 2010; Tumlinson et al. 2011; Rudie et al. 2012; Nielsen et al. 2013a, and references therein). Thus, the CGM represents an excellent laboratory for studying the processes which control galaxy evolution, containing remnants of past evolutionary processes and the fuel for future star formation.

Using background quasar sightlines probing gas traced by the Mg II $\lambda\lambda 2796, 2803$ absorption doublet (and other ion tracers), we now have a simple picture of the CGM in which gas accretes onto galaxies along their major axis to feed the ISM for future star formation (e.g., Steidel et al. 2002; Kacprzak et al. 2010a, 2012; Stewart et al. 2011; Danovich et al. 2012, 2015; Martin et al. 2012; Rubin et al. 2012; Bouché et al. 2013) and gas outflows along the minor axis to further pollute the CGM with metal-enriched gas (e.g., Rubin et al. 2010, 2014; Bouché et al. 2012; Kacprzak et al. 2012; Martin et al. 2012; Bordoloi et al. 2014b,a; Kacprzak et al. 2014; Schroetter et al. 2016). However, the large majority of this body of work has focused on an environment

in which only a fraction of galaxies are found: isolated environments. Absorbers associated with groups and clusters of galaxies have often been neglected and largely removed from the analyses.

Galaxy evolution is also environment-dependent. Even before the most complex parts of mergers occur, the signatures of galaxy–galaxy interactions are observable. Observations of cool H I gas show a variety of structures due to galaxy interactions in group environments, including tidal streams and filaments, warped disks, and high velocity clouds (e.g., Fraternali et al. 2002; Chynoweth et al. 2008; Sancisi et al. 2008; Mihos et al. 2012; Wolfe et al. 2013). Using the Illustris simulations, Hani et al. (2018) studied the impact of a major merger on the circumgalactic medium and found that the covering fraction of the largest column density gas increases pre-merger and remains elevated for several billion years post-merger. This effect was due to merger-driven outflows rather than tidal stripping. In the FIRE simulations, Anglés-Alcázar et al. (2017) also found that intergalactic transfer, particularly the transfer of gas from the outflows of one galaxy onto another nearby galaxy, is a dominant accretion mechanism of galaxies by redshift $z = 0$. These structures and the hierarchical processes that place them between galaxies are an additional level of complexity on top of the isolated galaxy CGM, yet understanding the CGM in these denser environments is necessary for understanding how galaxies grow and evolve. Just as the visible (emitting) portions of galaxies become tidally stripped and disturbed, so should the diffuse (absorbing) material in the CGM undergo complex interactions, and may do so before the visible galaxy due to the large radii involved.

In cluster environments, Lopez et al. (2008) studied Mg II

and found an overabundance of strong MgII absorbers that is more pronounced at lower impact parameters, suggesting that the halos of cluster galaxies are truncated at 10 kpc (also see Padilla et al. 2009; Andrews et al. 2013). The authors also found a relative lack of weak absorbers, which are expected to be more easily destroyed in clusters where the numbers are more consistent with those associated with isolated galaxies. Also on an extreme end are “ultrastrong” MgII absorbers with $W_r(2796) \geq 3 \text{ \AA}$. Without determining galaxy redshifts, Nestor et al. (2007) found evidence for a significant excess of galaxies around quasar sightlines hosting these absorbers compared to random fields, suggesting that group environments may give rise to some fraction of these extreme absorbers in addition to starbursts and very low impact parameter galaxies. Of the three ultrastrong MgII absorbers for which galaxy redshifts have been spectroscopically determined (Nestor et al. 2011; Gauthier 2013), all were found to be located in group environments and interpreted to be either outflows as the result of interaction-induced star formation, or tidal stripping.

In group environments, of which several have been studied, Chen et al. (2010) found that the equivalent widths of MgII absorbers in groups were similar to those associated with isolated galaxies, but they did not exhibit an anti-correlation between equivalent width and impact parameter, which has long been known for isolated galaxies (e.g., Lanzetta & Bowen 1990; Steidel et al. 1994; Kacprzak et al. 2008; Chen et al. 2010; Nielsen et al. 2013a). Using stacked galaxy spectra probing foreground galaxies, Bordoloi et al. (2011) found that MgII is more extended around groups, and this could be explained by a superposition of the equivalent widths of member group galaxies. Because of this superposition model, the authors suggest that the group environment (i.e., tidal stripping, interaction-induced star formation-driven outflows) does not appear to change the properties of MgII absorbers for individual galaxies. Finally, Whiting et al. (2006), Kacprzak et al. (2010b), Bielby et al. (2017), and Péroux et al. (2017) studied the absorption in one or two group environments each and concluded the gas was due to an intragroup medium or tidal interactions depending on the detailed characteristics of the sample. However, Rahmani et al. (2018) attributed the observed absorption to a single galaxy in the group, partially from the stellar disk and partially accretion onto a warped disk.

We focus on a sample of group galaxies compiled during our work to form the MgII Absorber–Galaxy Catalog (MAGIICAT; Nielsen et al. 2013a,b, 2015, 2016; Churchill et al. 2013b). Because of this, we did not actively seek out galaxies obviously undergoing mergers/interactions and therefore, the galaxies presented here are likely pre-merger but are still expected to show the effects of residing in more dense environments. While the galaxies themselves may not be obviously merging, their CGM is likely already affected by the group environment due to the large radius of the CGM out to roughly 200 kpc, compared to the visible (in emission) portions of the galaxies.

The paper is organized as follows: Section 2 describes our galaxy and quasar samples, along with our methods for creating a standardized catalog of group absorber–galaxy pairs. Section 3 details the properties of the group sample compared to the isolated MAGIICAT sample for the anti-correlation between MgII equivalent width and impact parameter while Section 4 examines the absorption kinematics with the pixel-

velocity two-point correlation function. These sections also report the results of a superposition model in which multiple galaxies contribute to the CGM of group galaxies. We examine the absorber Voigt profile cloud column densities and velocities in Section 5. Section 6 discusses the impact of the group environment on the CGM. Finally, Section 7 summarizes the work. We adopt a Λ CDM cosmology ($H_0 = 70 \text{ km s}^{-1} \text{ Mpc}^{-1}$, $\Omega_M = 0.3$, and $\Omega_\Lambda = 0.7$) and report AB absolute magnitudes throughout this paper. The group catalog presented here has been placed on-line at the NMSU Quasar Absorption Line Group website¹ along with the previously published isolated galaxy sample.

2. DATA AND METHODS

We compiled a sample of 29 MgII absorbers along 27 quasar sightlines and associated with a total of 74 foreground galaxies in group environments. The galaxies are located at $0.113 < z_{\text{gal}} < 0.888$ and within a projected distance of $D = 200 \text{ kpc}$ from the background quasar. An absorber is classified as being located in a group environment if there are two or more associated galaxies within a projected distance of 200 kpc and the galaxies have a line-of-sight velocity separation of less than 500 km s^{-1} . See Nielsen et al. (2013b, hereafter MAGIICAT I) for further discussion of our group environment criteria. While it is not one of the selection criteria, a majority of the groups in the sample are close ($\lesssim 50 \text{ kpc}$) pairs of galaxies with similar luminosities. Galaxy luminosities have a range of $0.01 < L_B/L_B^* < 2.49$ for all group galaxies or $0.15 < L_B/L_B^* < 2.49$ for only the most luminous galaxy in a group. Galaxy luminosity ratios (most luminous to second-most luminous) range from $1.01 < L_1/L_2 < 56.0$, where most have ratios below $L_1/L_2 = 10$.

In the following sections, we further describe the group sample and the sources of the data. We also describe the quasar spectra and their analysis.

2.1. Group Galaxy Sample

The group sample presented here was largely identified during our work to create the isolated galaxy sample in the MgII Absorber–Galaxy Catalog (MAGIICAT) where we either cataloged galaxies already identified as groups in the literature, or we identified new groups when consolidating multiple sources of data in the same fields. These galaxies are sourced from Steidel et al. (1994), Steidel (1996, private communication), Guillemin & Bergeron (1997), Steidel et al. (1997), Chen et al. (2010), Kacprzak et al. (2010b), Kacprzak et al. (2011a), and Kacprzak et al. (2011b). The surveys presented in each of these are detailed in MAGIICAT I. We obtained the published galaxy data for several more group environments from Whiting et al. (2006), Bielby et al. (2017), Péroux et al. (2017), Pointon et al. (2017), and Rahmani et al. (2018), and include new data for the Q1038+064 field, all of which we describe below. To summarize, the survey methods for these literature sources include absorption-selected samples, gas cross-section-selected samples (within a given impact parameter expected for MgII halos), “control fields” that were purposely targeted because absorption was not detected, magnitude-limited samples, and volume-limited samples.

There are additional groups published in Nestor et al. (2011) and Gauthier (2013), though they are classified as “ultrastrong” MgII absorbers ($W_r(2796) \geq 3 \text{ \AA}$). Due to their

¹ <http://astronomy.nmsu.edu/cwc/Group/magiicat>

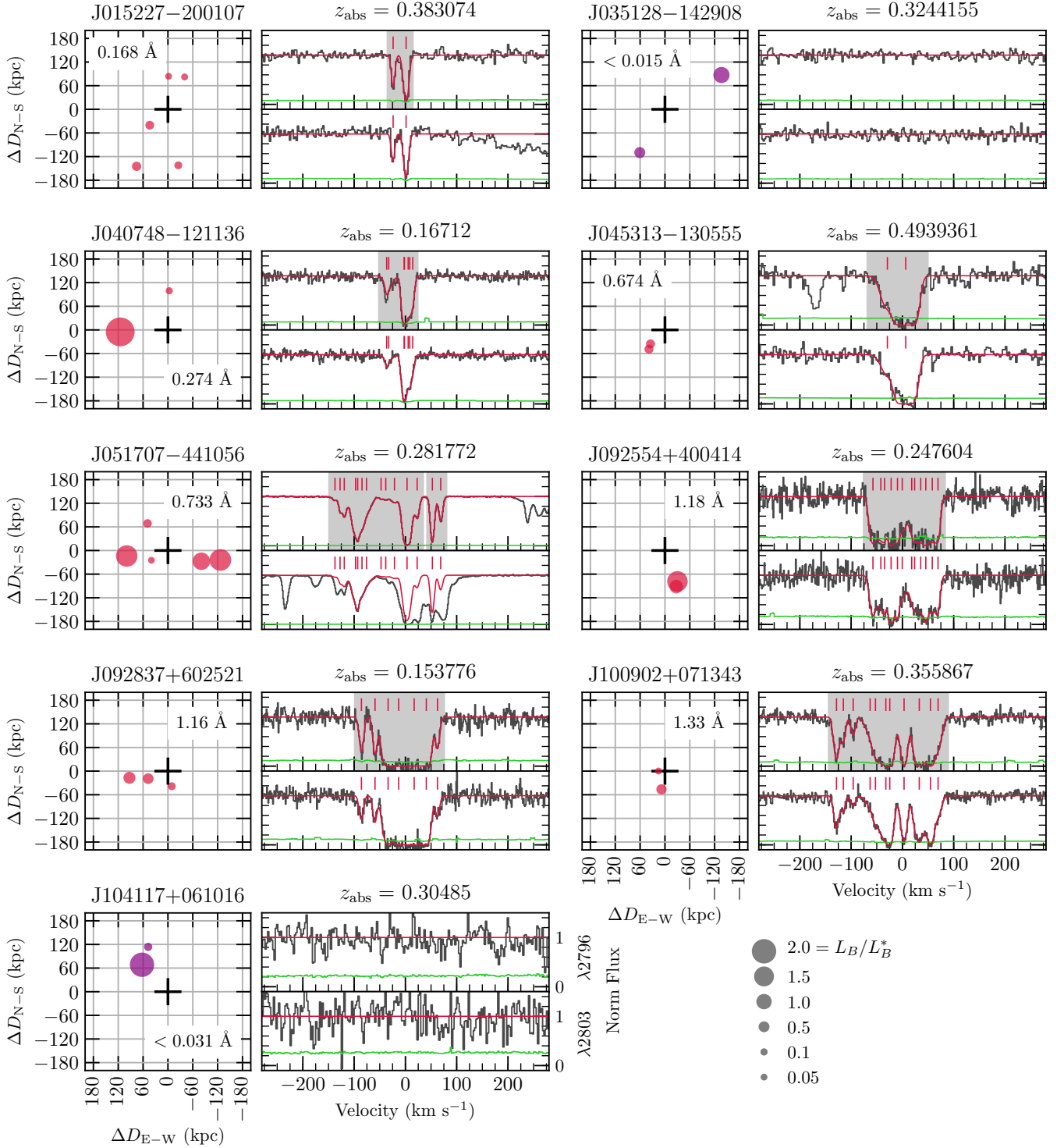


Figure 1. On-the-sky locations and absorption spectra for each group environment with measured Mg II absorption and a high-resolution HIRES/Keck or UVES/VLT spectrum. The left panel for each group shows the locations of each group galaxy (red and purple points) in physical space relative to the associated background quasar (black cross). Point sizes represent galaxy luminosity, L_B/L_B^* , with larger points representing more luminous galaxies. Red points represent those absorbers used in our kinematics analysis, while purple are not included in the kinematics analysis. The top panel in each spectrum panel pair shows the Mg II $\lambda 2796$ line, while the bottom panel shows the Mg II $\lambda 2803$ line. Black histograms are the data, red curves are the fit to the spectrum, red ticks are the individual Voigt profile components, and the green data are the error spectrum. Regions of the spectra where we use the pixel velocities for our kinematic analysis are highlighted in gray. The velocity zero points are determined by the optical depth-weighted median of absorption. Measured $W_r(2796)$ values are listed in the left panels for each group. We only have an upper limit on absorption for the J035128–142908 (Q0349–146) and J104117+061016 (Q1038+064) fields, and so there are no gray shaded regions.

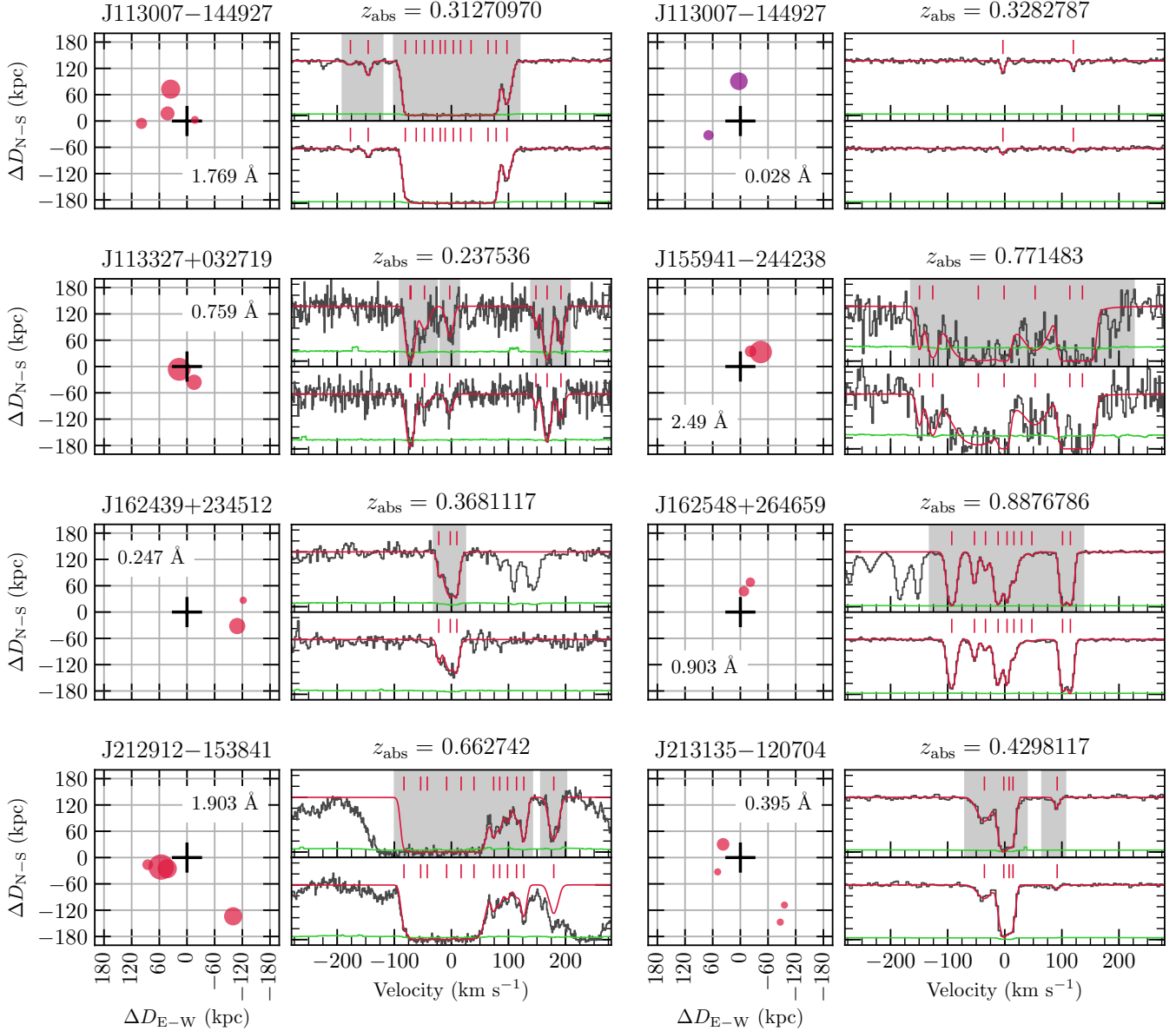


Figure 1. (continued) The absorber in J113007–144927 (Q1127–145), $z_{\text{gal}} = 0.328$ does not have gray shaded regions because the equivalent width of this absorber is below our equivalent width detection threshold, which we applied to ensure a uniform kinematic sample.

large equivalent widths and kinematic spreads, we therefore consider these absorbers outliers compared to the rest of our sample described below and this is further discussed in Section 6. We refrain from including these absorber–galaxy pairs in this sample and we also exclude the single isolated ultra-strong Mg II absorber from the isolated galaxy analyses.

2.1.1. Whiting et al. (2006)

Working with the known $z_{\text{abs}} = 0.663$ Mg II absorber in the PKS 2126–158 field (J212912–153841), Whiting et al. (2006) identified a group of galaxies at the redshift of absorption. The authors observed the field with the GMOS multi-object spectroscopy mode on Gemini South and imaged in the i' band. Galaxies were observed out to a field of view of $\sim 5'.5$ and down to a limiting magnitude of $i' = 24.6$. Eight galaxies were observed at $z \sim 0.66$, but only five were located within $D = 200$ kpc of the quasar sightline, and the redshift of one of the five galaxies is larger than our line-of-sight velocity sep-

aration criterion to be considered a group galaxy. We remeasured the equivalent width of this absorber in a UVES/VLT spectrum of the background quasar.

2.1.2. Bielby et al. (2017)

Observing with the Multi Unit Spectroscopic Explorer (MUSE) on the VLT, Bielby et al. (2017) spectroscopically identified a group of five galaxies in the HE0515–4414 (J051707–441056) field at the redshift of a $z = 0.282$ Mg II absorber. Galaxy apparent magnitudes were calculated in the R -band and the MUSE data cube has a 3σ depth of $f = 16 \times 10^{-18}$ erg cm $^{-2}$ s $^{-1}$ Å $^{-1}$. We obtained the UVES/VLT high signal-to-noise spectrum (Kotuš et al. 2017) and modeled the absorber following the methods described in Section 2.2 to be consistent with our previous work.

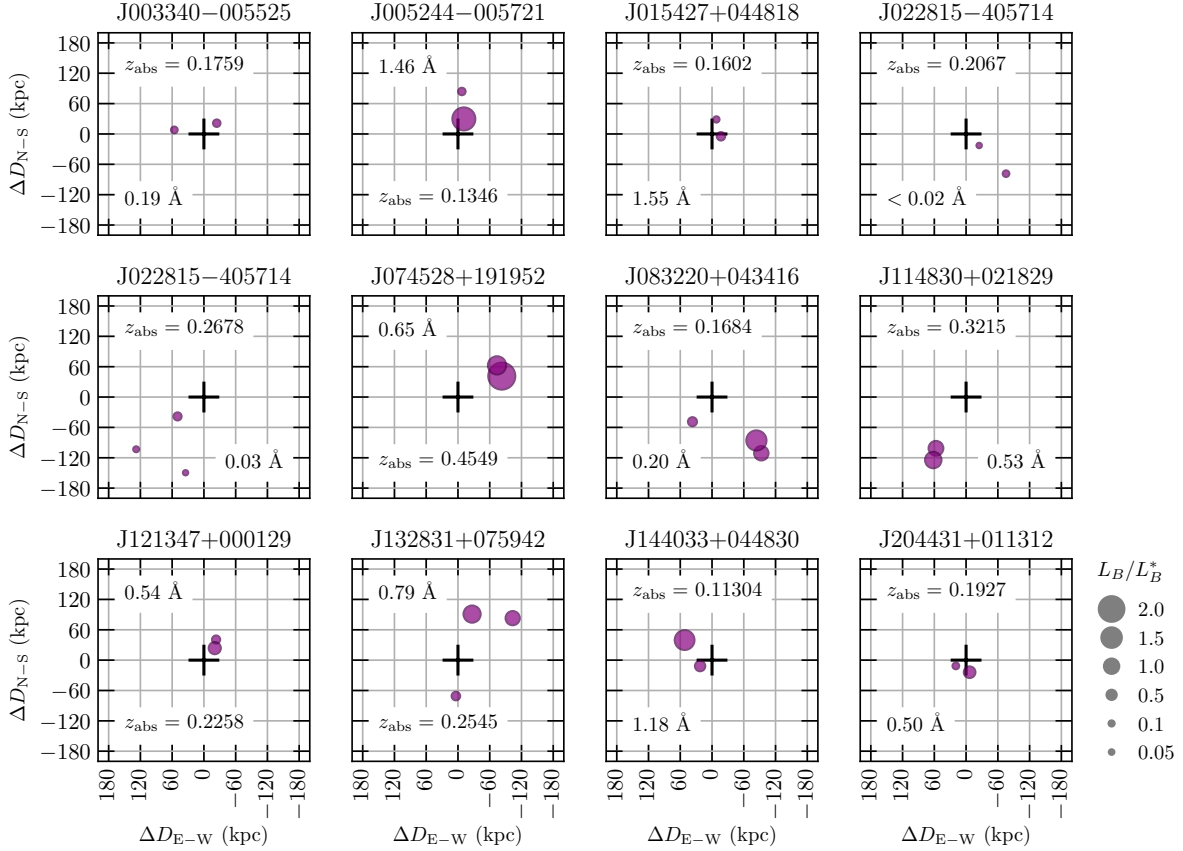


Figure 2. On-the-sky locations of each group galaxy in physical space for those groups in which we do not have high-resolution spectra of the associated background quasar. However, equivalent widths were measured for each associated absorber and are listed in Table 2 (including the measurement source), as well as on each panel. Purple points represent each galaxy in the group and the black cross represents the associated background quasar. Point sizes represent galaxy luminosity, L_B/L_B^* , with larger points representing more luminous galaxies. Galaxies in this Figure are not included in the kinematic TPCF analysis, but are included in Figures 3–5.

2.1.3. Péroux et al. (2017)

Péroux et al. (2017) observed the $z_{\text{abs}} = 0.4298$ absorber in the Q2128–123 field (J213135–120704) with MUSE/VLT to investigate the environment of the previously known absorber and its assumed isolated galaxy host. From two pointings with exposure times of 1200 s, the authors found an additional three low-luminosity ($L/L^* \sim 0.01$) galaxies at the redshift of the absorber. This field was classified as an isolated pair in MAGIIICAT I, but is now included in the present sample with the new findings. We remeasured the magnitudes of the two brightest galaxies in the group from a WFPC2/HST F207W image, but adopt the magnitudes and luminosities for the two faintest galaxies from Péroux et al. (2017) due to their being too faint to detect in the HST image.

2.1.4. Pointon et al. (2017)

The groups compiled by Pointon et al. (2017) were selected for having COS/HST spectra that covered the wavelength at which OVI absorption due to group environments was expected. From their sample, we selected groups for which HIRES/Keck and/or UVES/VLT spectra covered the Mg II doublet, regardless of whether absorption was detected, and measured the Mg II equivalent width or a 3σ upper limit on $W_r(2796)$. We also enforced the impact parameter and galaxy–galaxy velocity separation criteria for Mg II groups described in Section 2, which is more constraining than the OVI group criterion published by Pointon et al. (2017). The

galaxies drawn from this work were originally published in Chen et al. (2001), Chen & Mulchaey (2009), Meiring et al. (2011), Werk et al. (2012), and Johnson et al. (2013). From these works, we found three absorbers that were initially classified as isolated absorber–galaxy pairs in MAGIIICAT I, but have moved them to the group sample. These include the fields J022815–405714 ($z_{\text{abs}} = 0.2067, 0.2678$) and J035128–142908 ($z_{\text{abs}} = 0.3244$).

2.1.5. Rahmani et al. (2018)

Observing another previously known Mg II absorber assumed to be associated with an isolated galaxy (Q0150–202, J015227–200107, $z_{\text{abs}} = 0.383$), Rahmani et al. (2018) found an additional five galaxies with spectroscopic redshifts at the absorber redshift. The authors imaged the field with MUSE/VLT for a total of 100 min across two exposures, covering galaxies out to impact parameters of ~ 200 kpc. As already stated, this absorber–galaxy pair was previously identified as isolated in MAGIIICAT I, but we have moved the field to the present sample. Finally, we remeasured the galaxy magnitudes from a WFPC2/HST F702W image to be consistent with our measurements of the assumed isolated host.

2.1.6. Field Q1038+064

The $z_{\text{gal}} = 0.3044$ galaxy in this field (also known as J104117+061016) was identified, and its properties and associated quasar spectrum were provided to us by C. Steidel (1996, private communication). We obtained the spectrum

and spectroscopic redshift of the $z_{\text{gal}} = 0.3053$ galaxy with the Dual Imaging Spectrograph (DIS) on the Apache Point Observatory 3.5m telescope in March 2008 and the data were reduced using standard methods using IRAF.² This is one of only three group fields in the sample presented here to have only an upper limit on Mg II absorption measured.

2.1.7. Galaxy Properties

Details of the methods used to determine galaxy properties are described in full in MAGICAT I (Section 3.1 and the Appendices), as we compiled the majority of the group sample with the isolated sample. The galaxy properties obtained from the new group sample publications listed above were converted to AB B -band absolute magnitudes and luminosities and the Λ CDM cosmology ($H_0 = 70 \text{ km s}^{-1} \text{ Mpc}^{-1}$, $\Omega_M = 0.3$, and $\Omega_\Lambda = 0.7$) following the methods presented in MAGICAT I.

We obtained new galaxy spectra in eight fields (14 galaxies) with the Keck Echelle Spectrograph and Imager (ESI; Sheinin et al. 2002). Details of the data reduction are presented in Kacprzak et al. (2018), but the aim was to obtain accurate galaxy redshifts with precisions of $3 - 20 \text{ km s}^{-1}$. The ESI spectra have a resolution of $22 \text{ km s}^{-1} \text{ pixel}^{-1}$ when binned by two and cover a wavelength range of 4000 to 10,000 Å. Emission lines covered in this range include the O II doublet, H β , the O III doublet, H α , and the N II doublet. Galaxy spectra were vacuum and heliocentric velocity corrected for direct comparison with the absorption line spectra. Finally, the Gaussian fitting algorithm (FITTER; see Churchill et al. 2000) was used to determine the best-fit centroids and widths of the covered emission lines to determine galaxy redshifts.

Observed galaxy properties are tabulated in Table 1. The columns are: (1) QSO identifier, (2), Julian 2000 designation (J-Name), (3) galaxy spectroscopic redshift, z_{gal} , (4) quasar–galaxy right ascension offset, $\Delta\alpha$, (5) quasar–galaxy declination offset, $\Delta\delta$, (6) quasar–galaxy angular separation, θ , (7) reference for Columns 4, 5, and 6, (8) apparent magnitude used to obtain M_B , (9) band for the preceding apparent magnitude, (10) reference for Columns 8 and 9, (11) apparent magnitude used to calculate M_K , (12) band for m_K , (13) reference for Columns 11 and 12, and (14) galaxy SED type (from Coleman et al. 1980; Bolzonella et al. 2000) based on the galaxy observed color.

Calculated galaxy properties are tabulated in Table 2. Columns are: (1) QSO identifier, (2) Julian 2000 designation (J-Name), (3) galaxy spectroscopic redshift, z_{gal} , (4) Mg II absorption redshift, z_{abs} , (5) Mg II rest equivalent width, $W_r(2796)$, (6) Mg II doublet ratio, (7) reference for Columns 4, 5, and 6, (8) quasar–galaxy impact parameter, D , (9) K -correction to obtain M_B , (10) absolute B -band magnitude, M_B , (11) B -band luminosity, L_B/L_B^* , (12) K -correction to obtain M_K , (13) absolute K -band magnitude, M_K , (14) K -band luminosity, L_K/L_K^* , and (15) rest-frame color, $B - K$.

To illustrate their positions relative to each other and the quasar sightline, galaxies are plotted in RA and Dec (with physical distances) from the background quasar sightline (cross) in Figures 1 (square panels) and 2. Point sizes represent galaxy B -band luminosities, L_B/L_B^* , where larger points are more luminous galaxies.

2.2. Quasar Spectra

We have high-resolution quasar spectra for 16 fields (17 group environments) from HIRES on Keck or UVES on the VLT. Most of the spectra have been published elsewhere (Churchill 1997; Churchill & Vogt 2001; Evans 2011; Kacprzak et al. 2011b; Werk et al. 2013; Kotuš et al. 2017). The J155941–244238 quasar was observed specifically for this work in March 2013 with UVES on the VLT (programme number: 090.A-0304(A)) in the custom DIC2–470+760nm setting for a total exposure time of 2660s. The spectrum was reduced with the UVES pipeline (Dekker et al. 2000) and the exposures were combined and continuum fit with UVES_popler (Murphy 2016; Murphy et al. 2018).

To obtain the CGM absorption properties from these high-resolution spectra, the Mg II $\lambda\lambda 2796, 2803$ doublet absorption was modeled using one of two methods: (1) a combination of SYSANAL and MINFIT for six absorbers and (2) VPFIT for nine. The methods are summarized below.

The absorbers in the J045313–130555, J113007–144927, J162439+234512, J162548+264659, and J213135–120704 fields were modeled using SYSANAL and MINFIT, the methods for which are detailed in Churchill (1997), Churchill & Vogt (2001), Churchill et al. (2003), and Evans (2011). SYSANAL detects Mg II absorption with a 5σ (3σ) significance criterion in the $\lambda 2796$ ($\lambda 2803$) line following the formalism of Schneider et al. (1993). The code determines wavelength and velocity bounds where absorption is formally detected and calculates the rest-frame equivalent width, $W_r(2796)$. The absorption redshift, z_{abs} , is defined by the median wavelength of the apparent optical depth distribution of absorption. All systems are then fit using Voigt profile (VP) decomposition with MINFIT (Churchill 1997; Churchill & Vogt 2001; Churchill et al. 2003; Evans 2011) and the model with the fewest statistically significant VP components (clouds) is adopted. Cloud velocities, column densities, and Doppler b parameters are obtained from the MINFIT analysis.

For the remaining absorbers, J015227–200107, J040748–121136, J051707–441056, J092554+400414, J092837+602521, J100902+071343, J113327+032719, J155941–244238, and J212912–153841, we used VPFIT (Carswell & Webb 2014), and the full method is described in Pointon et al. (2017). Absorption redshifts are defined as the optical depth-weighted median of absorption as above and the velocity bounds of absorption were determined by finding the pixels at which the VP model decreases by 1% from the continuum level. The two fitting methods are comparable and do not result in any significant differences in our results.

The spectra and fits for each absorber are plotted in the second and fourth columns of Figure 1 for the 17 absorbers for which we have spectra. Black histograms are the data, red lines the model, green lines the error spectrum, and red ticks are the individual Voigt profile components. Shaded regions represent the velocity range of absorption for the $\lambda 2796$ line. Panels without shaded regions are either absorbers for which we have only a 3σ upper limit on absorption or the absorber has an equivalent width lower than the spectral equivalent width sensitivity limit of 0.04 \AA (see Nielsen et al. 2016, hereafter MAGICAT IV).

In cases where HIRES/Keck and/or UVES/VLT spectra are not available, we adopted the best published Mg II absorption values, typically the most recent measurements or those obtained from the highest resolution quasar spectra. These values and the references from which we obtained the values are

² IRAF is distributed by the National Optical Astronomy Observatory, which is operated by the Association of Universities for Research in Astronomy under cooperative agreement with the National Science Foundation.

tabulated in Table 2. Upper limits on absorption are quoted at 3σ .

2.3. Isolated Galaxy Sample

To test the influence that environment has on the CGM, we compare the group sample described above to our previously published isolated galaxy sample (MAGII CAT I). This sample has been modified to reflect new information on environments as detailed in Section 2.1 and to add the increasing number of spectroscopically-confirmed MgII absorber–galaxy pairs published in the literature. Thus MAGII CAT is a living catalog and its changes are periodically recorded on our publicly accessible website.³

3. EQUIVALENT WIDTH VS IMPACT PARAMETER

Here we examine the anti-correlation between equivalent width and impact parameter for the group galaxy sample described in the previous section compared to our isolated galaxy sample from MAGII CAT I.

3.1. $W_r(2796)$ vs. D : All Group Galaxies

A well-known relationship between the CGM and host galaxy properties is the MgII equivalent width anti-correlation with impact parameter, $W_r(2796)$ vs D (e.g., Lanzetta & Bowen 1990; Bergeron & Boissé 1991; Steidel 1995; Chen et al. 2010; Kacprzak et al. 2011b; Nielsen et al. 2013a,b). Figure 3 presents this anti-correlation for all group galaxies and the isolated galaxies from MAGII CAT I and Nielsen et al. (2013a), hereafter MAGII CAT II. Gray points and downward arrows correspond to the isolated galaxies and the solid and dashed gray lines are the log-linear fit and uncertainties to the isolated galaxy data from MAGII CAT II. Because the group sample has multiple galaxies associated with a single MgII absorber, there are galaxies at several impact parameters with the same $W_r(2796)$. The groups are identified by triangle points connected by horizontal lines. Point colors correspond to those in Figure 1, where red triangles are those groups for which we have high resolution quasar spectra and a measured equivalent width above an equivalent width completeness cut of 0.04 \AA . Purple points are the rest of the group sample.

From Figure 3 it appears that absorbers in group environments have larger equivalent widths at a given impact parameter than for the isolated sample. The median (mean) equivalent widths for the group and isolated galaxy samples are $\langle W_r(2796) \rangle = 0.65 \pm 0.13 \text{ \AA}$ ($0.75 \pm 0.11 \text{ \AA}$) and $\langle W_r(2796) \rangle = 0.41 \pm 0.06 \text{ \AA}$ ($0.62 \pm 0.05 \text{ \AA}$), respectively for the full sample. Upper limits on the equivalent width were considered “measurements” at the upper limit value. The median equivalent widths for the full group sample are larger than for the isolated sample (1.7σ).

The group environment sample contains only three groups in which only an upper limit can be measured on the MgII absorption equivalent width. We calculated the covering fraction, f_c , of the group environment and isolated galaxy samples for comparison, where we define the covering fraction as the fraction of absorbers with $W_r(2796)$ measurements to the total sample ($W_r(2796)$ measurements and upper limits). Upper limits are considered non-detections regardless of their value. The uncertainties on f_c are calculated using the formalism for binomial statistics (see Gehrels 1986). The covering fraction

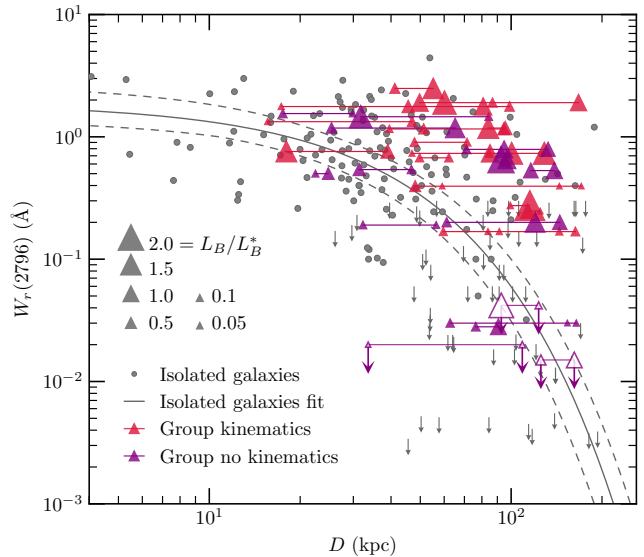


Figure 3. MgII equivalent width, $W_r(2796)$, as a function of impact parameter, D . Gray points represent absorbers (solid points) and non-absorbers (downward arrows) associated with galaxies in isolated environments. Purple and red triangles represent absorbers associated with galaxies in group environments, where the point sizes represent their B -band luminosity, L_B/L_B^* . For each group, we plot every galaxy in the group at the equivalent width of the absorber with a horizontal line drawn through each galaxy. Red triangles are those absorbers included in our kinematics analysis, while purple triangles are those for which we do not have a high-resolution spectrum of the background quasar or the measured equivalent width (including limits) is lower than our completeness cut of 0.04 \AA for the kinematics study.

of the group environment sample is $f_c = 0.89^{+0.05}_{-0.09}$ compared to $f_c = 0.68^{+0.03}_{-0.03}$ for the isolated sample, a 2.2σ difference. If we consider the groups J113007–144927, $z = 0.328$ and J022815–405714, $z = 0.2678$ as non-absorbers due to having equivalent widths smaller than the equivalent width sensitivity limit of 0.04 \AA , then the covering fraction reduces to $f_c = 0.82^{+0.07}_{-0.10}$, a 1.3σ difference. Group environments may be more likely to have associated MgII absorption than galaxies in isolation, although the result is only marginally significant. Note that Chen et al. (2010) examined a galaxy-selected sample and found only one non-absorbing group out of eight groups, which gives a covering fraction of $f_c = 0.87^{+0.10}_{-0.23}$ and is consistent with the values we obtain.

We also tested whether the galaxy properties for the group sample were any different from the isolated sample. KS tests comparing the redshifts, B -band luminosities, and $B-K$ colors (where available) of the group sample to the isolated sample show that the two samples are likely drawn from the same population ($< 3\sigma$). Conversely, the distributions of impact parameters for the group environment sample result in a significant KS test at the 3.4σ level, indicating that the null hypothesis that the two samples are drawn from the same population is disfavored. The group sample is located at larger impact parameters on average. However, note that the group sample in this case includes *all* group galaxies. If only one galaxy in the group actually hosts the absorption, regardless of whether it is the nearest galaxy or the most luminous, the KS test indicates that the impact parameter distributions between the group and isolated samples are likely drawn from the same population.

Since it is difficult to pinpoint which galaxy is giving rise to the observed absorption, several previous works have either assumed that the nearest galaxy (e.g., Steidel et al. 1994; Schroetter et al. 2016), or the most luminous/massive galaxy

³ <http://astronomy.nmsu.edu/cwc/Group/magiicat>

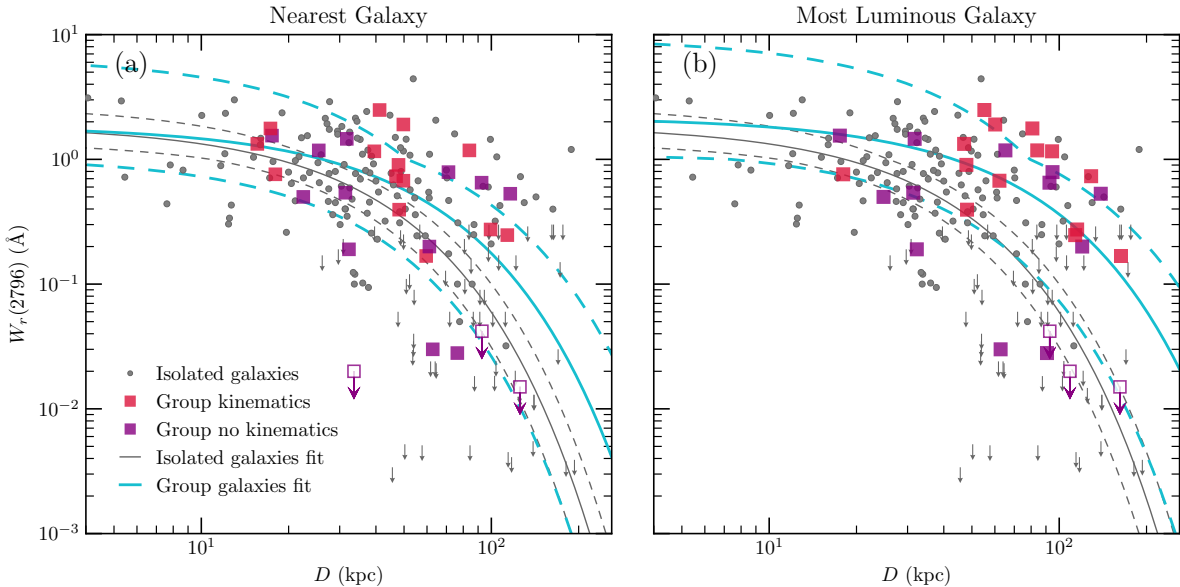


Figure 4. Mg II equivalent width, $W_r(2796)$, as a function of impact parameter, D , for (a) the galaxy nearest to the quasar sight-line and (b) the most luminous galaxy in the group. Isolated galaxies are represented by gray points and arrows, while group galaxies are squares. Square point colors are the same as the triangles in Figure 3. The gray solid and dashed curves are the expectation-maximization maximum-likelihood model and its 1σ uncertainties, respectively, published in Nielsen et al. (2013a) for the isolated galaxy sample. Cyan solid and dashed curves are the model and 1σ uncertainties, respectively, for the full group sample (red and purple points) plotted in each panel. The CGM for group environments has a similar distribution to isolated galaxies on the $W_r(2796)$ – D plane when the nearest galaxy is assumed to host the absorption, but the fitted slope may flatter when the most luminous galaxy in a group is assumed to host the absorption.

(e.g., Bordoloi et al. 2011; Schroetter et al. 2016) is the host galaxy. We further investigate the equivalent width anti-correlation with impact parameter by assuming that the absorption is either due to the nearest galaxy to the quasar sight-line (projected distance) or the most luminous galaxy.

3.2. $W_r(2796)$ vs. D : Nearest Galaxy

Selecting the nearest galaxy to the quasar as the source of the observed absorption has a historical basis, where Steidel et al. (1994) searched for galaxies giving rise to absorption by moving outwards in D and stopping with the first galaxy at an appropriate redshift. More recent work has conducted blind (to absorption) surveys of galaxies with nearby quasar spectra (e.g., Chen et al. 2010; Werk et al. 2013). Given the $W_r(2796)$ – D anti-correlation and the fact that the covering fraction decreases with increasing impact parameter (MAGIIICAT II), both for isolated galaxies, the nearest galaxy is more likely to give rise to the absorption, especially since the Mg II CGM radius is $\lesssim 200$ kpc.

Figure 4(a) presents the $W_r(2796)$ vs D anti-correlation for isolated galaxies (gray points and arrows) and group galaxies (square points), where D for the group environments is selected from the nearest galaxy to the quasar sightline in projected distance. The nearest galaxy for each group environment is shown in Figures 1 and 2 and the RA/Dec offsets and impact parameters for each galaxy are listed in Tables 1 and 2, respectively.

To test if there is an anti-correlation between equivalent width and impact parameter, we ran a non-parametric Kendall τ rank correlation test on $W_r(2796)$ against D for all of the square points in Figure 4(a), accounting for upper limits on absorption. We found a marginally significant result of 2.9σ , indicating that the two values may be anti-correlated, and that the equivalent width of absorption may decrease with increasing impact parameter. This is in contrast to the highly anti-correlated isolated sample with 7.9σ (MAGIIICAT II). The

CGM of group galaxies may have a flatter equivalent width profile than isolated galaxies. However, note that historically, this anti-correlation has not always been significant in the isolated sample. Only with larger samples (e.g., Chen et al. 2010; Kacprzak et al. 2011b, MAGIIICAT II) has the anti-correlation become statistically significant. Also note that the group environment sample has very few fields where only an upper limit on absorption can be measured, potentially biasing the sample to a flatter distribution. A larger group sample would be useful to investigate the level of bias and better determine how commonly group environments do not have associated Mg II absorption.

To test this further, we parameterized the nearest-galaxy group environment sample anti-correlation with the Expectation-Maximization maximum-likelihood method (Wolynetz 1979), accounting for upper limits on $W_r(2796)$. We fit a log-linear model similar to that for the isolated galaxies from MAGIIICAT II ($\log W_r(2796) = (-0.015 \pm 0.002) \log D + (0.27 \pm 0.11)$, gray solid and dashed lines). The group environment fit is shown as the cyan solid line, with 1σ uncertainties about the fit as dashed lines. The adopted fit to the group sample is $\log W_r(2796) = (-0.010 \pm 0.003) \log D + (0.35 \pm 0.42)$. This slope is slightly flatter than for the isolated sample (1.4σ) but the uncertainties are larger. The fit to the group data is consistent with the isolated sample within uncertainties so we cannot definitively state that the equivalent width profile of nearest-galaxy group environments is flatter than the isolated CGM. A larger group environment sample size may decrease the uncertainties on this fit.

3.3. $W_r(2796)$ vs D : Most Luminous Galaxy

Assuming the most luminous galaxy is giving rise to the detected absorption is also reasonable. As we found in Churchill et al. (2013a,b), more massive galaxies have a more extended CGM, where Mg II is regularly found out to $0.3R_{\text{vir}}$. Using luminosity as a proxy for mass, more luminous galaxies should

host a CGM that extends out to larger impact parameters, which we found in MAGIIICAT II. The most massive galaxies in a group will likely have the largest potential wells, allowing for the galaxy to host a more massive CGM. The covering fraction profiles also show that more luminous galaxies have a higher covering fraction than less luminous galaxies at a given impact parameter (MAGIIICAT II). For each group, we select the most luminous galaxy in the B -band. These galaxies are identified as the largest points in Figures 1, 2, and 3. The luminosities for each galaxy are also listed in Table 2.

Figure 4(b) presents the $W_r(2796)$ vs D anti-correlation for the most luminous group galaxy members. Point and line types and colors are the same as those in panel (a). The most luminous galaxies appear to have an even flatter distribution than what we found for the nearest galaxy sample. A rank correlation test (accounting for upper limits) on $W_r(2796)$ vs D results in only 2.6σ , less than for the nearest galaxy sample, although still marginally significant. We again fit the data with a log-linear model using the Expectation-Maximization maximum-likelihood method, accounting for upper limits on $W_r(2796)$. The adopted fit to these data is $\log W_r(2796) = (-0.007 \pm 0.002) \log D + (0.33 \pm 0.25)$. The slope for the most luminous galaxies is flatter than for the isolated galaxy sample (2.8σ), but the full fit is not significantly different. Assuming the most luminous galaxy in a group gives rise to the observed absorption, the group Mg II CGM may be more extended than the isolated CGM.

Since we selected the most luminous group galaxies, there may be biases causing the flatter fit to the data than with the isolated sample. However, we ran a KS test comparing the luminosities of the galaxies in this most luminous group galaxy sample to the isolated sample and found that the two samples were drawn from the same population (1.9σ). We also compared the impact parameters of the two samples and found no significant difference (2.2σ).

3.4. $W_r(2796)$ vs D : Superposition Model

Using stacked galaxy spectra to probe the CGM of foreground galaxies, Bordoloi et al. (2011) found that the possible extension of the group CGM distribution can be modeled by a superposition of absorption profiles associated with individual galaxies. This method assumes that the individual galaxies are not affected by galaxy–galaxy interactions in the groups, but that the larger equivalent widths are simply due to the quasar sightline piercing multiple circumgalactic media. To test this, the authors summed the equivalent widths associated with isolated galaxies according to the modeled fit to the isolated galaxies on the $W_r(2796)$ – D plane and the impact parameter distribution of the group members in question. Because the resulting superposition model is consistent with the group data, they suggested that the observed absorption is simply due to a superposition of individual halos and that the group environment may not affect the Mg II CGM of individual galaxies. We investigate this further using our distribution of MAGIIICAT isolated galaxies.

For each group, we substitute equivalent width measurements from isolated galaxies within similar impact parameters to remove the potential impact of galaxy–galaxy interactions on the observed absorption profiles. We first identify galaxies from our isolated galaxy catalog within ± 8 kpc of each group galaxy member. This impact parameter range was selected to be as small as possible so that the $W_r(2796)$ – D anti-correlation does not change drastically over the D range, but large enough to contain at least five isolated galaxies. With

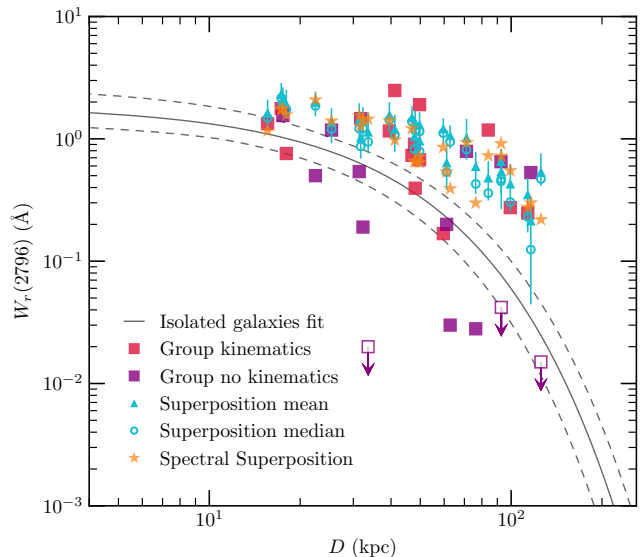


Figure 5. Superposition model for each group environment, where the impact parameter is defined by the group galaxy nearest to the quasar sightline. The choice of galaxy for the impact parameter does not affect the results. Gray lines and square points are plotted as in Figure 4(a). Cyan symbols and lines are the summed equivalent widths from the CGM of multiple galaxies (see Section 3.4 for details). Triangles are the mean equivalent width values and the circles the median values for 1000 realizations in a bootstrap analysis. Vertical blue lines indicate the 1σ uncertainty around the mean equivalent width from the bootstrap analysis to take into account the scatter in the isolated galaxy sample. Orange stars are superposition model equivalent widths calculated from summed absorption profiles (see Section 4.2.2). The superposition model fits well with some of the group environments, but misses the lowest equivalent width groups.

this sample, we randomly draw an isolated galaxy within the impact parameter range for each group galaxy member and sum the associated equivalent widths with the assumption that upper limits on absorption are “absorbers” at the measured upper limit value. This is done 1000 times for each group using a bootstrap analysis in which we randomly draw new isolated galaxy replacement equivalent widths for each realization, and the mean and median of the summed equivalent widths and 1σ uncertainties from all of the bootstrap realizations are calculated. This method therefore takes into account the spread in the isolated galaxy distribution on the equivalent width–impact parameter plane, and does not depend on the fit applied to the isolated sample in this plane (as is the case in Bordoloi et al. 2011).

The results of this superposition model are shown in Figure 5, where the point colors and types are similar to those in Figure 4(a). The choice of plotted galaxy impact parameter does not affect the results of this analysis because we are comparing total equivalent widths and take into account the group galaxy member impact parameters in the equivalent width summation. Therefore, we choose the nearest galaxy for simplicity. The cyan triangles (circles) are the mean (median) equivalent width of the bootstraps for the superposition model, while the vertical lines indicate the 1σ uncertainties in the bootstraps to show the range in possible summed equivalent widths. The superposition model fits half of the data well, but misses the lower equivalent width groups. The model points still lie within the scatter of the isolated points, but tend toward the upper right portion of the distribution. Given that the model does not explain all of the groups, especially those with low equivalent widths, it is likely that not all group member galaxies contribute to the absorption in all cases.

Because summing equivalent widths does not take into account the reality that gas associated with multiple galaxies may be located at the same line-of-sight velocities, and therefore the model equivalent widths may be overestimated, we also calculate superposition model equivalent widths by summing absorption spectra (for full details, see Section 4.2.2). This method accounts for galaxy–galaxy velocity separations due to slightly different galaxy redshifts across the group and for absorber–galaxy velocity separations due to gas motions around individual galaxies. The resulting summed equivalent widths are presented as orange stars in Figure 5. There are some variations in the calculated values due to the fact that we can only use the subset of isolated galaxies for which we have the associated quasar spectrum. Regardless, the equivalent widths derived from the absorption spectra are similar to those derived by summing equivalent width values.

With this superposition modeling, we also investigated the expected covering fraction, f_c , of the group environment sample by keeping track of the number of absorbers and non-absorbers (upper limits on absorption) in each bootstrap realization. For a group in the superposition model to be a non-absorber, all galaxies in that group must not have measurable absorption, i.e., upper limits on absorption must be randomly drawn for every galaxy in the group. For a galaxy to be classified as an absorber, at least one galaxy must have absorption. The mean covering fraction expected from this model is $f_c = 0.83^{+0.03}_{-0.01}$, where the uncertainties are 1σ uncertainties in the bootstrap realizations from the mean. The value is comparable to that found for the actual group environment sample within uncertainties ($f_c = 0.89^{+0.05}_{-0.09}$), but is significantly larger than the isolated galaxy sample ($f_c = 0.68^{+0.03}_{-0.03}$). This suggests that absorption is more likely to be found in group environments in a superposition model than for isolated galaxies alone. The result that the superposition covering fraction is lower than the actual value (despite being within uncertainties) also suggests that the superposition model may be too simplistic by neglecting galaxy–galaxy interactions.

4. KINEMATICS

The equivalent width of an absorber is proportional to the number of clouds fit with Voigt profile modeling (e.g., Petitjean & Bergeron 1990; Churchill et al. 2003; Evans 2011). The group galaxies appear to have a more extended CGM, where group galaxies may have a larger $W_r(2796)$ at a given D than isolated galaxies, at least for scenarios in which the most luminous group galaxy hosts the observed absorption. This indicates that the absorber velocity spread, column density (and thus the metallicity, path length, ionization conditions, etc.), or some combination may be larger for group environments. Therefore, we investigate the kinematics of the group absorbers using the pixel-velocity two-point correlation function (TPCF).

The TPCF is defined as the probability distribution function of the velocity separation of every absorbing pixel pair in a sample. Full details of the pixel-velocity TPCF method are published in MAGII CAT IV (also see Nielsen et al. 2015, 2017). To create the TPCF, we obtain the pixel velocities in every absorber (defined by the velocity bounds of absorption, see Section 2.2) for a sample. Absorption regions (and their associated pixel velocities) that have equivalent widths less than our completeness cut of 0.04 \AA are not included in this analysis. We then calculate the velocity separations of each possible pixel pair in a given sample, without repeats. The

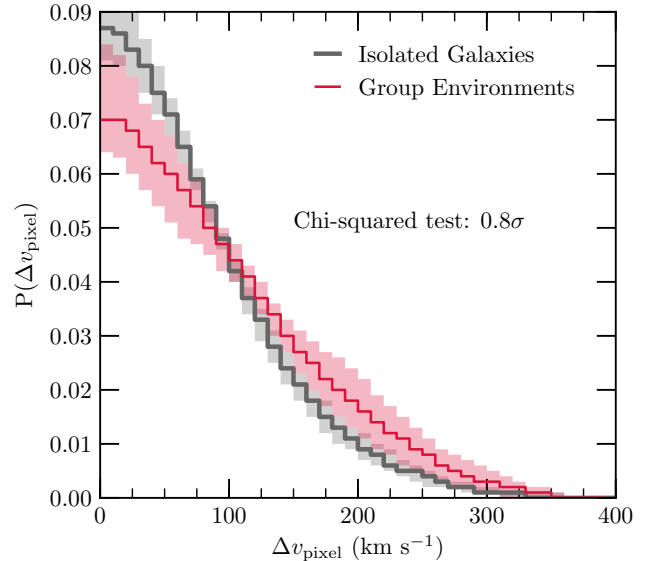


Figure 6. Pixel-velocity two-point correlation functions (TPCFs) comparing absorbers associated with isolated galaxies (thick gray line and shading) to absorbers associated with galaxies in group environments (thin red line and shading). The samples contain all absorber–galaxy pairs in our sample with high-resolution quasar spectra. The histograms represent the TPCF, while the shaded regions are the uncertainties on the TPCF from a bootstrap analysis. Absorbers associated with galaxy groups have statistically similar velocity dispersions as those associated with isolated galaxies (0.8σ). However, the group sample has more power at $\Delta v_{\text{pixel}} \sim 200 \text{ km s}^{-1}$, which may be due to the superposition of the CGM of multiple galaxies, tidal interactions, or intergalactic transfer.

absolute value of the velocity separations is calculated, and these values are binned in 10 km s^{-1} bins. The count in each bin is then normalized by the total number of pixel-velocity pairs in the sample to create a probability distribution function.⁴ The TPCF is roughly a measure of the velocity dispersion of absorbers in a given sample. Note that TPCFs can be created for only those galaxies/groups in which absorption is detected; nonabsorbers do not provide kinematic information due to the lack of pixels contributing to observed absorption.

Uncertainties on the TPCF are calculated using a bootstrap analysis. We randomly draw, with replacement, the same number of absorbers from the sample in question and calculate the TPCF for that realization. We do this for 100 realizations and calculate the mean and standard deviation of the realizations. The uncertainties we plot are 1σ bootstrap uncertainties.

We calculated the TPCF for both our group sample with high-resolution quasar spectra (red points in Figure 1) and for our isolated galaxy sample with high-resolution quasar spectra presented in MAGII CAT IV. There are 14 group environments and 46 isolated galaxies involved in the TPCF calculations. The median redshifts for the samples are tabulated in Table 3. The TPCFs are presented in Figure 6, where the red curve and shaded region are the TPCF and uncertainties, respectively, for the group sample. Isolated galaxies are plotted as a gray curve and shaded region.

From Figure 6, we find that absorbers associated with galaxies in group environments have statistically similar velocity dispersions as those associated with isolated galax-

⁴ For the samples presented here, there are roughly 3 million (isolated galaxy sample) and 500,000 (group environment sample) pixel-velocity pairs in the TPCF calculations.

Table 3
TPCF $\Delta v(50)$ and $\Delta v(90)$ Measurements

Sample	# Gals	$\langle z_{\text{abs}} \rangle$	$\Delta v(50)^b$	$\Delta v(90)^b$
Isolated Galaxies	46	0.656	66^{+3}_{-4}	177^{+9}_{-9}
Group Environments	14	0.411 ^a	79^{+13}_{-11}	199^{+22}_{-27}
Galaxy–Galaxy Groups	10	0.443	85^{+12}_{-15}	208^{+20}_{-35}
Galaxy–Dwarf Groups	4	0.330	60^{+8}_{-34}	139^{+20}_{-68}

^a Median redshift measured only from the group galaxies with high-resolution quasar spectra (red points in Figures 1 and 3).

^b km s^{-1}

ies, where a chi-squared test comparing the TPCF distributions of the group galaxy sample to the isolated galaxies results in a significance of 0.8σ . We further characterize the TPCFs by determining the TPCF velocity separation, Δv_{pixel} , within which 50% and 90% of the velocity separations are located, $\Delta v(50)$ and $\Delta v(90)$, respectively. These values are $79^{+13}_{-11} \text{ km s}^{-1}$ and $199^{+22}_{-27} \text{ km s}^{-1}$ for the group environment sample, respectively, and $66^{+3}_{-4} \text{ km s}^{-1}$ and $177^{+9}_{-9} \text{ km s}^{-1}$ for the isolated galaxy sample, respectively. These values are also tabulated in Table 3. The $\Delta v(50)$ and $\Delta v(90)$ values for the group sample are both larger than for the isolated sample, although the uncertainties overlap. The TPCFs for both samples generally extend out to the same velocity separation of $\sim 350 \text{ km s}^{-1}$, but the group TPCF has more power at $\sim 200 \text{ km s}^{-1}$ than the isolated TPCF. Larger velocities would be expected in a group superposition of halos and/or where interactions between group galaxies are occurring. We investigate this further in the following sections.

4.1. Galaxy–Galaxy Luminosity Ratios

If we assume that the absorption properties are due to galaxy–galaxy interactions, there may be some observable differences due to the type of environment, which we quantify by calculating the luminosity ratio of the two brightest galaxies in a group. A majority of the sample presented here involves pairs of galaxies with similar luminosities that are close in projection. In these environments, the CGM (and the galaxies themselves) are expected to be impacted more dramatically by interactions than environments where there is a large galaxy and one or more “dwarf” galaxies. Thus we investigate this effect by slicing the sample by the luminosity ratio between the two brightest galaxies in each group, assuming the B -band luminosity is a proxy for galaxy mass. We define galaxy–galaxy groups as those where the ratio between the two brightest galaxies (most luminous over second-most luminous) is $L_1/L_2 < 3.5$, regardless of the impact parameter between the two galaxies. Galaxy–galaxy groups may result in a future major merger. Galaxy–dwarf groups are defined as group environments where the ratio is $L_1/L_2 \geq 3.5$, and these may result in a future minor merger.

The median equivalent width for galaxy–galaxy groups, $\langle W_r(2796) \rangle = 0.74 \pm 0.17 \text{ \AA}$ (mean $0.87 \pm 0.14 \text{ \AA}$), is 1.7σ (1.8σ) larger than for galaxy–dwarf groups, $\langle W_r(2796) \rangle = 0.27 \pm 0.21 \text{ \AA}$ (mean $0.48 \pm 0.17 \text{ \AA}$). Out of the three non-absorbing groups in the sample, two are classified as galaxy–dwarf groups, while one is a galaxy–galaxy group, resulting in covering fractions of $f_c = 0.95^{+0.04}_{-0.11}$ (galaxy–galaxy) and $f_c = 0.78^{+0.14}_{-0.22}$ (galaxy–dwarf), which are consistent within uncertainties. These results suggest that the kinematics and/or

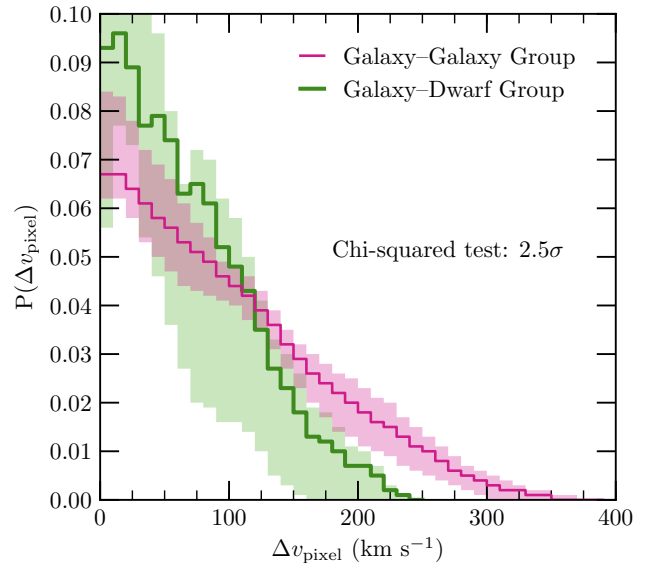


Figure 7. Gas kinematics comparing galaxy–galaxy groups ($L_{B,\text{ratio}} < 3.5$; pink) and galaxy–dwarf groups ($L_{B,\text{ratio}} \geq 3.5$; green). Absorption associated with galaxy–galaxy groups may have larger velocity dispersions than absorption associated with galaxy–dwarf groups. Although this result is only marginally significant at the 2.5σ level, largely due to the galaxy–dwarf subsample containing only four groups, the galaxy–dwarf uncertainties trend towards narrower velocity dispersions.

column densities of absorbers depends on the group galaxy luminosity ratio, potentially hinting at interaction/merger effects.

Figure 7 presents the TPCFs comparing galaxy–galaxy and galaxy–dwarf groups for only the absorbers in the subsamples (recall that there is no kinematic information in non-absorbers). Galaxy–galaxy groups host absorbers with a larger velocity dispersion than galaxy–dwarf groups, but the result is only marginally significant (2.5σ) due to the large uncertainties in the galaxy–dwarf sample. Regardless, groups in which a major merger may occur in the future (galaxy–galaxy) appear to drive the kinematic trends in the group environment TPCF.

4.2. Kinematics Superposition Modeling

If the superposition model presented in Section 3.4 and in Bordoloi et al. (2011) for the equivalent width of absorption associated with group galaxies is accurate, then the model should also apply to the kinematics of these absorbers. Here we apply the superposition technique to create model absorbers and use these to calculate TPCFs for three different cases. These cases include (1) the absorption is “stacked” where the absorption due to multiple galaxies all lies at the same redshift (z_{abs}); (2) the absorption is truly associated with individual galaxies, where the kinematics depend on both the galaxy–galaxy velocity distributions of each group and the absorber–galaxy velocity distribution expected for each member galaxy to reflect their individual baryon cycles; and (3) the absorption is due to a common intragroup medium in which the gas is observed at a common velocity with small velocity offsets due to random gas motions.

In each case we work only with those absorbers (and upper limits on absorption) for which we have high-resolution quasar spectra in order to obtain the detailed kinematics. For instances where only an upper limit is measured in these spectra, the (non-)absorption does not contribute to the TPCF be-

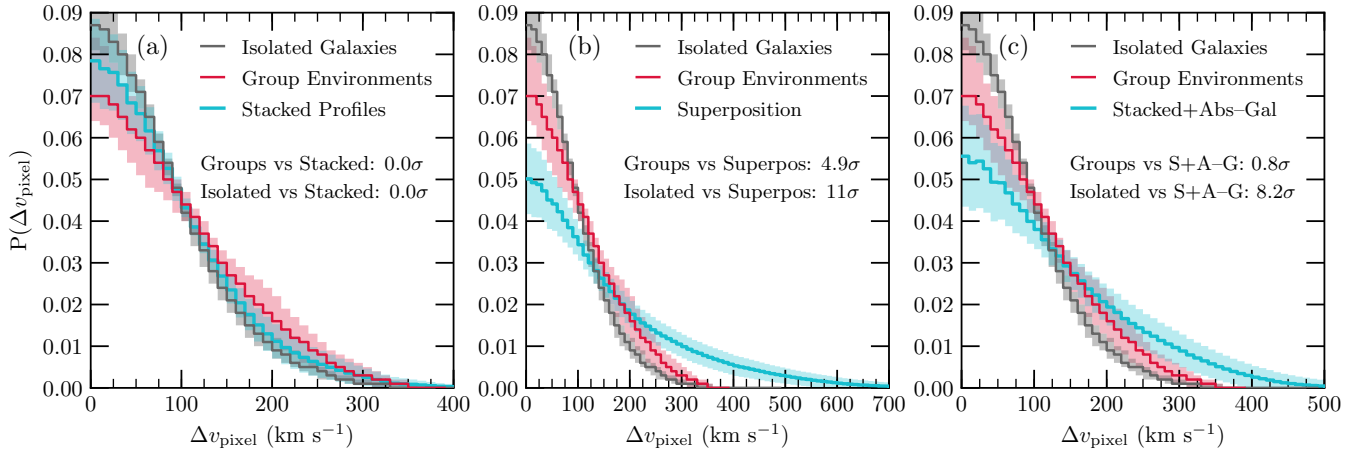


Figure 8. Superposition modeling for the group environment pixel-velocity TPCF. In each panel, the gray lines and shading represent the isolated sample while the red lines and shading represent the group sample, both previously plotted in Figure 6. The cyan lines and shading are the TPCFs for three different superposition model cases: (a) Case 1: A simple stack of absorption profiles creates a TPCF that is consistent with the isolated TPCF (0σ) and the group TPCF (0σ). (b) Case 2: A proper superposition of halos that includes both absorber–galaxy and galaxy–galaxy velocity offsets for the model absorption profiles results in a TPCF that is inconsistent with both the group TPCF (4.9σ) and the isolated TPCF (11σ). (c) Case 3: A stack of absorption profiles, where each contributing absorber is shifted from a common redshift (absorber–galaxy velocity offsets), is comparable to the group environment TPCF (0.8σ) but not the isolated galaxy TPCF (8.2σ).

cause there are no pixels contributing to absorption in these cases. Though note that the covering fraction of the individual group member contributions is often less than one, and in many cases no absorption is modeled for entire group environments.

4.2.1. Case 1: Stacked Profiles TPCF

For the first case, we created stacked absorption profiles by randomly selecting isolated galaxies within ± 8 kpc of each galaxy in a group and obtained the absorption profiles associated with each. We rebinned every profile onto a common velocity array with 3 km s^{-1} pixel widths to match the resolutions of the HIRES and UVES spectrographs. These rebinned absorption profiles are then summed in velocity space, where $v = 0 \text{ km s}^{-1}$ is the optical depth-weighted median of the summed absorption (z_{abs}). This assumes that the individual group galaxy absorption contributions are centered at the same redshift regardless of the spread in group galaxy redshifts or any offset the absorption might have from the host galaxy. This may be interpreted as an intragroup medium with more absorbing material at a given line-of-sight velocity than in an isolated environment. Each group has its own summed absorption profile with contributions from each group member galaxy. The summed absorption profiles for each group were then used to calculate a TPCF. This analysis was done for 1000 bootstrap realizations where the random selection of isolated galaxies that go into the superposition model are bootstrapped, and the mean and standard deviation in each bin of the TPCF realizations were calculated.

Figure 8(a) presents the isolated and group TPCFs from Figure 6, with the addition of the stacked profiles TPCF in cyan. The mean of the stacked profiles TPCF bootstrap realizations is plotted as the cyan line, while the 1σ standard deviation of the realizations is plotted as the cyan shaded region. We find that this “stacked” TPCF is consistent with both the isolated sample (chi-squared test: 0σ) and the group sample (0σ), though it is still narrower than the group sample. The larger uncertainties on the stacked TPCF compared to the isolated TPCF, despite being drawn from the same samples, is likely due to the random nature of the analysis and the smaller

group galaxy sample size compared to the isolated sample (14 versus 46). This stacked profiles model is a useful exercise since it represents the minimum velocity spreads possible in a superposition scenario. However, this model is unrealistic because it neglects the relative motions of gas around individual galaxies due to baryon cycle processes, as well as the relative velocities between group member galaxies. Therefore, the model is ruled out.

4.2.2. Case 2: Superposition TPCF

In the second case, we conduct a similar analysis as the previous section, but now adopt realistic galaxy and gas velocity shifts. Before we sum the individual absorbers, the absorbers are shifted in velocity for both: (1) Absorber–galaxy velocity offset based on the Gaussian distribution of velocity offsets presented in Chen et al. (2010), with $\langle v_{\text{abs-gal}} \rangle = 16 \text{ km s}^{-1}$ and $\sigma_{\text{abs-gal}} = 137 \text{ km s}^{-1}$; and (2) Galaxy–galaxy velocity offset based on the distribution of group galaxy redshifts. The redshift of the group galaxy with the smallest impact parameter in the field defines $v = 0 \text{ km s}^{-1}$ for simplicity, with additional galaxies having velocity offsets from that. We randomly draw absorber–galaxy velocity offsets from the Chen et al. (2010) Gaussian distribution for each group galaxy. These velocity shifts combined more accurately represent the distribution of gas expected if the absorption is truly associated with individual galaxies in the group and if the gas is not influenced by or coupled to other group members. The group member absorption profile contributions are then summed, and the total absorption redshift, z_{abs} , and absorption velocity bounds are recalculated. The TPCF analysis then proceeds as above.

The result of this analysis is presented in Figure 8(b). The superposition TPCF is plotted in cyan, while the isolated and group samples are plotted as before. The resulting TPCF has a velocity dispersion that is much too large compared to the true group sample (chi-squared test result: 4.9σ). If we do not shift the absorbers according to the absorber–galaxy velocity offset distribution (velocity shift number 1 above), the TPCF comparison is slightly more extended and inconsistent with the group TPCF at the 5.0σ level. This exercise suggests that the hypothesis in which each group galaxy may contribute

separately to the observed absorption profile is incorrect. This is largely due to the spread in group galaxy redshifts and indicates that the observed gas is coupled to the group environment or 1-2 galaxies rather than every individual galaxy in the group. Thus the superposition model appears to be incorrect.

4.2.3. Case 3: Absorber–Galaxy Velocity Offsets TPCF

The third case assumes that there is a common intragroup medium in which multiple galaxies contribute gas but the individual contributions are offset slightly from a common redshift. In this case, we assume all contributing absorbers start with $v = 0 \text{ km s}^{-1}$ representing z_{abs} for each absorber (like the stacked spectra TPCF above), and then randomly shift these velocities individually according to the absorber–galaxy velocity offset presented by Chen et al. (2010). Then we sum the absorption profiles, redefine z_{abs} and velocity bounds for the new summed profile, and then proceed with the TPCF calculation. This method is similar to the superposition model in the preceding section, except we do not include galaxy–galaxy velocity separations, which dominate the kinematic spread.

The resulting TPCF is presented in Figure 8(c), where lines, shading, and colors are similar to the previous panels. The stacked, absorber–galaxy velocity offset TPCF (presented as the cyan line and shading) is comparable to the group environment sample, with a chi-squared test result of 0.8σ , however the tail on the model TPCF appears to be too extended. Compared to the isolated sample, the model TPCF has a velocity dispersion that is too large (8.2σ). This result and the previous two superposition model scenarios suggest that an intragroup medium as the physical region giving rise to the observed Mg II gas is more plausible than a true superposition of galaxy halos model.

4.2.4. Other TPCFs

Curiously, the group environment TPCF is consistent with presumably outflowing gas in the isolated galaxy subsamples published in Nielsen et al. (2015, hereafter MAGIIICAT V). These subsamples are subsets of the isolated galaxy catalog presented as gray symbols and lines in all figures so they have galaxy properties (redshifts, impact parameters, luminosities, etc.) that are consistent with the group environment sample. In Figure 9 we present a comparison between the full group environment sample (red) and the isolated face-on, minor axis sample (cyan) from MAGIIICAT V. The latter subsample consists of face-on galaxies ($i < 57^\circ$) probed along the minor axis ($\Phi \geq 45^\circ$) by the quasar sightline, which is expected to be the orientation at which outflows are best measured. A chi-squared test comparing this TPCF and the group environment sample results in a significance level of 0.0σ . Due to the complexity of gas flows in group and interacting environments, it is unlikely that the gas observed in the group environment sample is (solely) due to outflowing gas, especially in a statistical sense as is the case for the TPCFs. However, this TPCF comparison does suggest that the processes responsible for the properties of this group gas may disturb the gas similarly to outflows through tidal stripping, or even induce outflows.

In MAGIIICAT V, we explored several more subsamples sliced by galaxy orientation properties and galaxy color to better understand the processes traced by Mg II absorption. For orientations in which outflows are expected to dominate the observed absorption signatures, the kinematics are consistent with the group sample. For those orientations in which outflows are non-existent or where accretion is expected to

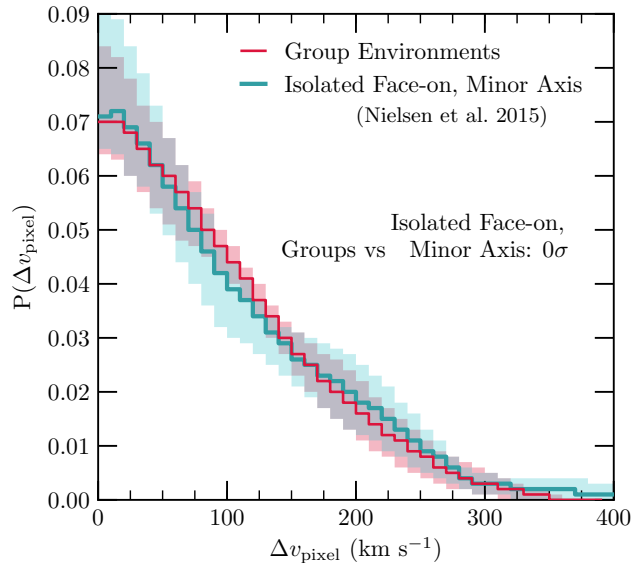


Figure 9. TPCF for absorbers associated with isolated face-on ($i < 57^\circ$, minor axis ($\Phi \geq 45^\circ$) galaxies from MAGIIICAT V (cyan thick line and shading) compared to the full group environment (red line and shading) sample. The face-on, minor axis galaxy sample is a subset of the full isolated galaxy sample where the subsample’s kinematics were associated with outflows in MAGIIICAT V. The kinematics for absorbers found in group environments are comparable to those along the minor axis of face-on, isolated galaxies. This suggests that the gas probed by Mg II in group environments is either outflowing material, or is agitated similarly to outflows (potentially streams from tidal stripping).

dominate, the kinematics are inconsistent with the group environment sample.

5. CLOUD COLUMN DENSITIES AND VELOCITIES

To examine the “clumpiness” of the absorbers along the line of sight, we plot the column densities and velocities of each VP fitted cloud component in the top panel of Figure 10. Red triangles represent the VP modeled clouds for the group sample with high-resolution quasar spectra and gray circles are those for the full isolated sample from MAGIIICAT IV. The left histograms show the distribution of cloud column densities for the two samples, while the bottom histograms show the distribution of pixel velocities (note that the points in the scatter plot show *cloud* velocities, which are represented by the red ticks at the top of the absorption profile panels in Figure 1). Showing the pixel velocities gives a more accurate picture of the velocity spread of the absorbers and are the values used to calculate the TPCFs. In both histogram sets, thin red lines represent the group sample and thick gray lines are the isolated sample.

Overall, the VP model cloud column densities and velocities for the group sample do not differ significantly from the isolated sample. The highest velocity clouds tend to have small column densities and the highest column density clouds have the smallest velocities, a result that largely reflects the velocity zero point definition (absorption redshift). There is the exception of a few group sample clouds at $v_{\text{pixel}} \geq 100 \text{ km s}^{-1}$ and $\log N(\text{Mg II}) = 14 - 16$. A KS test comparing the cloud column density distributions indicates that the two samples are drawn from the sample population at the 1.3σ level. Lower limits on the column densities are considered measurements at the value of the limit.

However, the pixel velocities for the two samples are different: an F -test comparing the variance in the distributions rules

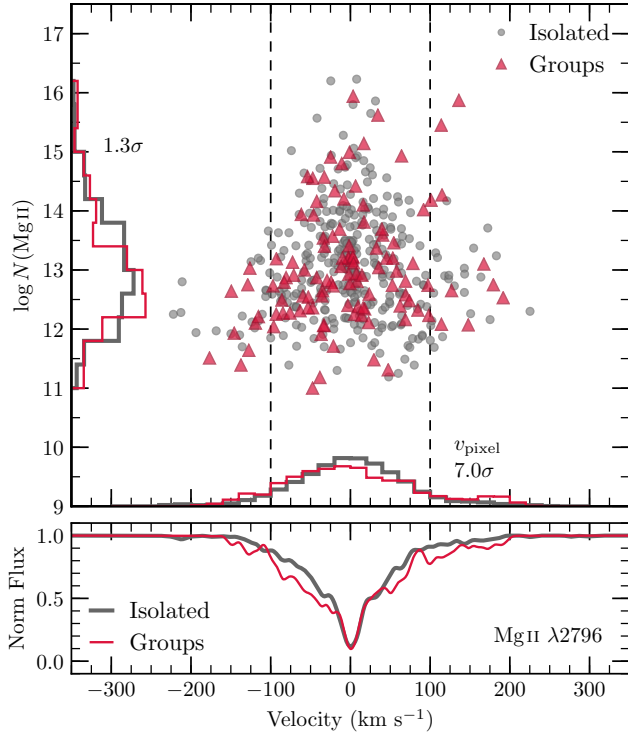


Figure 10. (Top) VP model cloud column densities and velocities comparing group environments (red triangles and thin lines) to isolated galaxies (gray circles and thick lines). Histograms compare the distributions of the cloud column densities (left axis) and pixel velocities (bottom axis) for the two samples, normalized by the number of points in each sample. Vertical dashed lines at $v = \pm 100$ km s $^{-1}$ are plotted to guide the eye. The cloud column densities are comparable between the group and isolated samples, but the group sample has a significantly higher fraction of $v \geq 100$ km s $^{-1}$ clouds (16.8%) than the isolated sample (13.5%). (Bottom) Average model spectra for the group environments (red) and isolated galaxies (gray).

out the null hypothesis that the two samples are drawn from the same population at the 7.0σ level. The pixel velocities for the group sample have a flatter distribution and are more extended than for the isolated sample, similar to the TPCFs.

The group sample also has a significantly (3.3σ) higher fraction of “high velocity” ($v \geq 100$ km s $^{-1}$) clouds than the isolated sample, with $16.8_{-0.8}^{+1.7}\%$ for the groups compared to $13.5_{-0.9}^{+0.6}\%$ for the isolated sample. The 1σ uncertainties on these fractions were calculated by conducting a bootstrap analysis over 1000 realizations in which cloud velocities from each sample were randomly drawn with replacement and new fractions were determined. For only galaxy–galaxy groups ($L_1/L_2 < 3.5$), the fraction increases to $19.5_{-1.1}^{+2.3}\%$. These “high velocity” clouds contribute to the increased number of pixel velocity separations of ~ 100 – 200 km s $^{-1}$ in the group TPCF compared to the isolated TPCF. However, the group and isolated samples have similar numbers of clouds per absorber on average, with $n_{\text{clouds}} = 8.1 \pm 1.1$ for the groups sample compared to $n_{\text{clouds}} = 7.1 \pm 0.7$ for the isolated sample. Restricting the group sample to galaxy–galaxy groups, we find $n_{\text{clouds}} = 8.7 \pm 1.4$, which is larger but still consistent within uncertainties.

To test if there is more material along the line of sight in group environments (i.e., the absorbing gas has a larger physical distribution, has a higher density, or some combination of the two) due to probing the CGM of two or more galaxies, we compare the total column densities of ab-

sorbers found in group environments to those in isolated environments. The median (mean) total column densities are $\log N(\text{Mg II}) = 14.20 \pm 0.32$ (14.25 ± 0.26) for groups and $\log N(\text{Mg II}) = 13.89 \pm 0.18$ (14.21 ± 0.15) for isolated galaxies. These values are consistent within uncertainties. For only galaxy–galaxy groups, we find $\log N(\text{Mg II}) = 14.40 \pm 0.41$ (14.41 ± 0.33), which is still consistent within uncertainties with the isolated sample. If the quasar line-of-sight is probing two or more galaxies as expected in a superposition model, we would expect the group environment column densities to be about 0.3 dex larger than the isolated sample (assuming the absorption from both halos have similar column densities). This may not be the case (though note that the uncertainties are also ~ 0.3 dex), which could either indicate the individual halos contribute different amounts of gas or the superposition model is incorrect. A KS test comparing the total column density distributions for the group (galaxy–galaxy group) and isolated samples results in a significance of 0.03σ (0.2σ), thus we cannot rule out that the two samples were drawn from the same population. This indicates that the amount of material observed along the line of sight may be similar in group and isolated environments.

Finally, we plot the average model absorption spectra for the group (thin red line) and isolated (thick gray line) samples in the bottom panel of Figure 10. We use the model spectra (red lines in Figure 1) to remove any contributions to the average spectra from noise and blends. Comparing the two samples, we find that the average absorption spectra are similarly concentrated at $v = 0$ km s $^{-1}$, but the average group absorption spectrum has more optical depth on average at higher velocities, particularly $v \gtrsim 100$ km s $^{-1}$. The reader may be concerned that higher velocity components in the isolated sample are washed out due to averaging the absorption spectra for 46 absorbers, whereas the group sample is only averaging 14 absorbers. However, a bootstrap analysis on the isolated sample with 5,000 realizations of 14 randomly drawn isolated absorbers (without replacement) found that these realizations are rarely consistent with the group average absorption spectrum. In fact, 3σ bootstrap uncertainties on the average absorption profile for isolated galaxies are plotted, but they are on the order of or smaller than the line thickness. Therefore, the dilution of isolated galaxy absorption features does not appear to be an issue. However, a larger group environment sample would be beneficial to further examine this.

6. DISCUSSION

The previous sections show that, statistically, Mg II absorbers in group environments have absorption properties that are largely comparable to their isolated counterparts within uncertainties. The median equivalent width is 1.7σ larger than for isolated galaxies and the anticorrelation between equivalent width and impact parameter may be flatter depending on which galaxy is assumed to host the absorption. Group environments have larger CGM covering fractions than isolated galaxies (2.2σ). The kinematics of gas in group environments have similar velocity dispersions compared to those in isolated environments, although the group sample has a higher fraction of high-velocity clouds (VP components) fitted to the absorbers. Group absorbers have more optical depth at larger line-of-sight velocities. Finally, the velocity dispersions and median equivalent widths for galaxy–galaxy groups ($L_1/L_2 < 3.5$) are marginally larger than for galaxy–dwarf groups ($L_1/L_2 \geq 3.5$), although the covering fractions are consistent.

To better understand the underlying physics involved, we tested the superposition model of [Bordoloi et al. \(2011\)](#) on equivalent widths and kinematics and found that this model generally appears to explain the larger equivalent width systems in the group sample. When studying the absorber kinematics in a superposition model, simply stacking absorption profiles appears to model the group TPCF extended velocity dispersion. However, the resulting TPCF is unrealistic since it neglects both the relative velocities between group member galaxies and the absorber–galaxy velocities due to baryon cycles associated with individual galaxies. Therefore, we rule this model out. A proper kinematic superposition of CGM gas in which these velocity shifts are accounted for results in velocity dispersions that are much too large. These two models bracket the group sample and indicate that the superposition model is too simplistic, especially since group environments likely have the added complication/confusion of galaxy–galaxy interactions.

Previous work looking at individual group environments favored various scenarios giving rise to the observed absorption. For example, [Kacprzak et al. \(2010b\)](#) found two groups in the Q1127–145 field. For the larger equivalent width group at $z_{\text{abs}} = 0.313$, the authors suggested that the absorption was due to tidal tails and streams bridging the group galaxies. This is supported by the observation of perturbed morphologies for three of the brightest galaxies in the group, with possible tidal streams extending out to at least ~ 25 kpc in deep *HST* imaging. For the other group in the field at $z_{\text{abs}} = 0.328$, the galaxies do not appear to have perturbed morphologies, have similar metallicities, and the gas has a low Mg II equivalent width. The origin of this weaker absorption is therefore ambiguous and the authors did not assign any scenario to explain this gas.

[Whiting et al. \(2006\)](#) found eight galaxies associated with strong absorption, all of which appeared to be early-type galaxies. The authors concluded that absorption associated with so many early-type galaxies was rare, and they could not rule out intragroup gas as the source of absorption. In their preferred scenario, galaxy interactions remove gas from the individual galaxies and deposit the gas into an intragroup medium. More recently, [Bielby et al. \(2017\)](#) identified five galaxies in MUSE observations associated with a strong absorber. The authors also preferred an intragroup medium scenario in which the gas is accreting onto the overall group halo, and suggested that this material may have been sourced from the accretion/outflow of material from individual galaxies that mixed into the group environment. This latter scenario is described as a “superposition” by the authors, but one in which galaxy interactions do not contribute to the overall intragroup halo.

By studying the environments of two previously known isolated absorbers with MUSE, both [Péroux et al. \(2017\)](#) and [Rahmani et al. \(2018\)](#) found additional galaxies at the redshift of the known absorbers. In the former work for the Q2128–123 field, one galaxy in the group is significantly more luminous than the rest ($L_1/L_2 = 56$, a galaxy–dwarf group here) and at the lowest impact parameter to the quasar sightline. The authors found that the gas was largely associated with this most luminous, nearest galaxy, either as co-rotating halo material, and/or as accretion. They also suggest that some portion of the observed gas is associated with an intragroup medium. In the latter work, [Rahmani et al. \(2018\)](#), the authors studied the Q0150–202 field and also conclude that the observed absorption is associated with the galaxy nearest to the quasar sightline, although it is not the most lu-

minous in the group. Based on the gas kinematics and galaxy morphology information, the authors conclude that this gas is also co-rotating and potentially accreting in a warped disk. Both of these absorbers have Mg II equivalent widths significantly less than the median equivalent width of the group sample, where the superposition model in [Figure 5](#) does not match the observed equivalent widths.

Based on the results presented in the previous sections and considering that the absorber–group pairs detailed in the previous paragraphs are included in the present sample, we also support an intragroup medium scenario where one or more galaxies contribute material, but also one in which galaxy interactions play some part in distributing the gas throughout the group halo rather than a general superposition of multiple galaxy halos scenario. The degree to which each of these contributions participate in shaping the intragroup material largely depends on individual circumstances of the groups in question as shown above. However, we are examining the impact of the group environment in a statistical manner and are less concerned with the particulars, which we leave to other work. We arrive at our favored scenario for the following reasons:

First, the $W_r(2796) - D$ superposition model in [Section 3.4](#) generally agrees with the equivalent widths for the largest equivalent width groups. This would indicate that the largest equivalent width absorbers have (on average) larger column densities, larger velocity spreads, or some combination of both due to probing multiple unrelated halos of gas. However, the median total column densities for the isolated and group samples for which we have quasar spectra (basically the kinematics subsample) are consistent within uncertainties. Additionally, the kinematics in [Section 4](#) show that the group environment and isolated galaxy TPCFs are consistent within uncertainties, although there is increased optical depth at larger velocities in the group sample. Examining the group environment sample in more detail, the kinematics may depend on the luminosity ratio of the two brightest galaxies in the group (the result is only marginally significant due to large uncertainties in the galaxy–dwarf group sample), suggesting that interactions may play a role in distributing the observed gas in velocity space.

Second, the over-prediction of the low equivalent widths in the $W_r(2796) - D$ superposition model ([Section 3.4](#)) may also indicate a more complicated CGM in group environments than assumed. In this scenario, the covering fraction around some individual group galaxies may be less than expected in a superposition model, which does account for the non-absorption present in the isolated sample. Perhaps the ionization conditions or metallicities of the gas are less consistently conducive to the presence of Mg II absorption than in isolated galaxies even though multiple galaxies are available to contribute absorbing material. However, the column densities (which depend on ionization conditions, metallicities, and path lengths) for the group sample are statistically comparable to the isolated sample, suggesting that this is not the case. Alternatively, and perhaps more simply, not every galaxy in the group contributes to the absorption and the observed gas is more associated with an intragroup medium rather than individual galaxies.

Third, the superposition model does not accurately represent the absorption kinematics. A proper superposition that includes galaxy–galaxy and absorber–galaxy velocity offsets results in a TPCF with a velocity dispersion that is much larger than what is observed. This is largely due to the galaxy–

galaxy velocity offsets, which we confine to $\Delta v \leq 500 \text{ km s}^{-1}$ in our group definition. Therefore, the observed gas is likely coupled to the group (intragroup medium) rather than individual member galaxies. Given that the group environment kinematics are comparable to those associated with isolated face-on galaxies probed along their minor axis (presented in MAGIIICAT V), this suggests that the intragroup material is either outflowing material from one or more galaxies, or is agitated similarly to outflows. This is also strengthened by the fact that the average absorption spectrum for group environments has larger optical depth at higher velocities than the average isolated sample absorption spectrum. For a given line-of-sight velocity $v \gtrsim 50 \text{ km s}^{-1}$, group absorbers have either more gas, more metal-rich gas, larger path lengths, or some combination compared to isolated galaxies, but are similar in the cores of the absorption profiles. If this is outflowing material, the fact that the gas appears to be coupled to the group may suggest that it is gas undergoing an “intergalactic transfer” by way of wind transfer as described by [Anglés-Alcázar et al. \(2017\)](#) in the FIRE simulations (see also [Oppenheimer & Davé 2008](#); [Kereš et al. 2009](#); [Oppenheimer et al. 2010](#)). In this scenario, gas is transferred between nearby galaxies via outflowing winds and is an accretion mode that dominates the accretion of gas onto L^* galaxies by $z = 0$.

Another possible explanation is that tidal stripping may agitate the gas in similar ways. The [Anglés-Alcázar et al. \(2017\)](#) simulations suggest that gas stripping from galaxy interactions is less important than intergalactic transfer except for the later stages of galaxy mergers. We did not specifically target galaxies clearly undergoing interactions and the later stages of mergers. However, warps and potential tidal streams are directly observed in deep *HST* images of at least one group in the sample (Q1127–145, $z_{\text{abs}} = 0.313$; [Kacprzak et al. 2010b](#)). Also, because of the large radius of the CGM in comparison to the visible portions of the host galaxy, we would expect interactions to start changing CGM properties of the participating galaxies before the visible galaxy portions become more obvious. Thus we cannot rule out gas stripping and streams as the source of Mg II absorption in groups.

There are further suggestions that merger/interaction activity is giving rise to the observed group absorption. We examined the properties of absorbers associated with galaxy–galaxy groups (i.e., the two brightest galaxies in a group have similar luminosities, $L_1/L_2 < 3.5$) and those in galaxy–dwarf groups ($L_1/L_2 \geq 3.5$). Comparing the two, we found that absorbers in galaxy–galaxy groups may have larger velocity dispersions and equivalent widths than in galaxy–dwarf groups, although the result is only marginally significant. The covering fractions are consistent within uncertainties, with galaxy–galaxy groups trending toward larger fractions. This result suggests that not only do galaxy–galaxy interactions affect the CGM, but the type of interaction/environment may influence the absorption properties. Groups in which major mergers occur (galaxy–galaxy groups) may be more likely to cause tidal stripping of CGM gas and/or induce star formation in both galaxies involved. In the most dense environments of clusters, [Lopez et al. \(2008\)](#) found an overabundance of strong Mg II absorbers whereas weak absorbers are destroyed (see also [Padilla et al. 2009](#); [Andrews et al. 2013](#)). Combining our results with more dense environments, we suggest that the group environment may enhance the absorption strengths and kinematics, but once the environment becomes too dense, and therefore too hot, this effect is reduced and the weakest ab-

sorbers are eventually ionized to higher states. Further work is needed to investigate this turn-over point for Mg II.

It is interesting that the group sample has only three non-absorbers, with the rest having measurable absorption. This results in a covering fraction of $f_c = 0.89_{-0.09}^{+0.05}$ for the group environment sample, in contrast to $f_c = 0.68_{-0.03}^{+0.03}$ for the isolated galaxy sample. If the superposition model is correct in that multiple galaxies contribute to the observed absorption, then a larger covering fraction in group environments would be expected. In our superposition modeling, we in fact found a superposition covering fraction of $f_c = 0.83_{-0.01}^{+0.03}$ for the group environments, which is consistent within uncertainties with the observed group environment covering fraction. More importantly, this covering fraction is significantly larger than that found in the isolated sample. Despite the superposition model matching the observed group covering fraction, it still does not accurately represent the observed kinematics. These results combined further point to an intragroup medium for these group environments (or more accurately, galaxy pairs in most cases), where tidal stripping and intergalactic transfer is common for populating the CGM with low-ionization, kinematically complex gas.

A potential bias in comparing the group and isolated environment samples for the kinematics analysis is that the galaxies in the group environment sample are located at a lower redshift on average than the isolated sample: 0.411 versus 0.656, respectively, for the kinematics sample only. However, in MAGIIICAT IV we found that the kinematics are consistent for blue galaxies at low and high redshift (split by $\langle z_{\text{gal}} \rangle = 0.656$) and the velocity dispersion decreases from high to low redshift for red galaxies. If this redshift bias were affecting the present analysis, the TPCFs for the group environment sample would either remain constant or be more narrow than the isolated sample. This is not the result we find; the gas kinematics in the group environment sample are comparable to or more active than for the isolated sample. As stated in Section 3, a KS test comparing galaxy properties (impact parameters, luminosities, colors, and redshifts) between the two samples indicates that the null hypothesis that they were drawn from the same population cannot be ruled out, so the galaxies themselves do not appear to be different between samples with the information we have available.

We have left out the sample of ultrastrong Mg II absorbers associated with group environments found by [Nestor et al. \(2011\)](#) and [Gauthier \(2013\)](#) because they are outliers in equivalent width and because we do not have their spectra. Additionally, the Nestor et al. absorbers were identified in low-resolution SDSS spectra, in contrast to the high-resolution HIRES and UVES spectra for the sample presented here. If these absorbers were included in the sample, the mean equivalent widths, absorber velocity dispersions, covering fractions, median column densities, and number of clouds would all increase, in some cases making the group environment sample no longer consistent with isolated galaxies. For example, if we include only the [Gauthier \(2013\)](#) absorber (4.2 Å) in the kinematics analysis, the resulting TPCF would be significantly more extended out to $\sim 550 \text{ km s}^{-1}$. However, we do not include these absorbers in the sample because they are extreme outliers in every absorption property. It is possible that these ultrastrong Mg II absorbers are more likely hosted by group environments due to their unique physical processes – out of the isolated MAGIIICAT sample of ~ 180 galaxies, only one is an ultrastrong absorber. Previous work has

attributed these absorbers to starburst-driven outflows from interactions and/or from stripped material in the intragroup medium. However, further work needs to be done with these absorbers to better understand their origin.

Finally, the behavior of the low ionization Mg II doublet in group environments differs from that of the intermediate, CIV, and higher, OVI, ions. Recently, Pointon et al. (2017) showed that OVI associated with group galaxies similar to those presented here has lower equivalent widths and a more narrow TPCF than around isolated galaxies. Also, the covering fraction of OVI in groups is less than Mg II groups. The authors suggested that, similar to the results in the EAGLE simulations by Oppenheimer et al. (2016), OVI is more sensitive to the virial temperature and therefore the ionization conditions of the host halo. Since group galaxies are hosted by more massive halos, the absorbing gas is ionized to higher ionization states, resulting in less observed OVI absorption. A similar result was found with CIV by Burchett et al. (2016) at $z < 0.015$, where the detection rate for CIV drops to zero when there are more than seven galaxies in the group environment (for cluster environments, see Burchett et al. 2018). They also found that the column densities appear to be influenced by their host mass/environment, similar to the OVI and Oppenheimer et al. work, but that CIV may continue to be observed in overdense regions due to containing more gas from galaxy–galaxy interactions. In comparison, we have shown that Mg II in groups (2–5 galaxies) may have larger covering fractions and equivalent widths, and more optical depth at large line-of-sight velocities compared to absorbers around isolated galaxies. This suggests that Mg II may be less sensitive to the ionization conditions of the host halo than the higher ionization states. Upon reaching cluster sizes, Mg II halos are truncated and only the weakest absorbers are destroyed (Lopez et al. 2008; Padilla et al. 2009; Andrews et al. 2013). This further suggests that the low and intermediate/high ions trace different components of the CGM (e.g., Werk et al. 2013, 2016; Ford et al. 2014; Churchill et al. 2015; Muzahid et al. 2015; Stern et al. 2016; Nielsen et al. 2017; Pointon et al. 2017) and emphasizes that a multiphase approach to studying the CGM is necessary to fully understand the dominant mechanisms involved.

7. SUMMARY AND CONCLUSIONS

We presented the Mg II Absorber–Galaxy Catalog (MAGII-CAT) group sample to complement the isolated sample presented in our MAGII-CAT papers (Nielsen et al. 2013a,b, 2015, 2016; Churchill et al. 2013b). The group sample consists of 29 Mg II absorbers associated with group environments along 27 quasar sightlines for a total of 74 foreground galaxies. The sample is located at $0.113 < z_{\text{gal}} < 0.888$ and within $D = 200$ kpc of a background quasar sightline. A group is defined as having two or more galaxies within a projected distance of 200 kpc and with a velocity separation of less than 500 km s^{-1} . With this sample, we examined the absorption properties as a function of galaxy environment and find the following:

1. The median equivalent widths for the group environment sample ($0.65 \pm 0.13 \text{ \AA}$) are larger than for isolated galaxies ($0.41 \pm 0.06 \text{ \AA}$) (1.7σ).
2. The equivalent width vs impact parameter anti-correlation may be flatter for galaxies in group environments than those in isolated environments, where a rank correlation test is marginally significant for the group

environment sample at 2.9σ compared to 7.9σ for isolated galaxies. If we assign the most luminous galaxy in the group as the absorber host, then the slope of the $W_r(2796) - D$ fit is significantly flatter than for isolated galaxies. The slopes are consistent within uncertainties when the group galaxy nearest to the quasar sightline is assumed to host the observed absorption.

3. The covering fraction of Mg II in group environments, $f_c = 0.89^{+0.05}_{-0.09}$, are larger than for isolated galaxies, $f_c = 0.68^{+0.03}_{-0.03}$, although this is marginally significant at the 2.2σ level.
4. Using the pixel-velocity TPCF method to study absorber kinematics, we found that while the velocity dispersion of absorbers in group environments is consistent within uncertainties compared to those in isolated environments (0.8σ), the group kinematics trend towards larger dispersions with more power at $\Delta v_{\text{pixel}} = 200 \text{ km s}^{-1}$.
5. The type of merger activity may influence the CGM properties. Groups in which the two brightest galaxies have similar luminosities (galaxy–galaxy; $L_1/L_2 < 3.5$) have 1.7σ (1.8σ) larger median (median) equivalent widths and larger absorber velocity dispersions (2.5σ) than in galaxy–dwarf groups ($L_1/L_2 \geq 3.5$). However, their covering fractions are comparable within uncertainties, with $f_c = 0.95^{+0.04}_{-0.11}$ for galaxy–galaxy groups and $f_c = 0.78^{+0.14}_{-0.22}$ for galaxy–dwarf groups.
6. The distribution of fitted cloud column densities are consistent within uncertainties between the group and isolated samples. Absorbers in the group sample have a comparable number of clouds but a significantly (3.3σ) larger fraction of high velocity clouds, $v \geq 100 \text{ km s}^{-1}$, than for the isolated sample. When only galaxy–galaxy group environments are compared to the isolated sample, the fraction of high velocity clouds in groups is increased.
7. A superposition of individual group galaxy CGM results in equivalent widths that are comparable to the measured values in the group sample for the strongest absorbers. The model also finds a covering fraction of $f_c = 0.83^{+0.03}_{-0.01}$, which is similar to the observed values. However, the superposition model is too simplistic to explain the observed TPCF (kinematic) distributions, where a proper superposition results in absorption velocity dispersions that are much too large.
8. The group absorber kinematics appear similar to the kinematics of presumably outflowing gas around face-on galaxies probed along their minor axis (see MAGII-CAT V). This suggests that the gas in group environments may be agitated similarly to that entrained in outflowing winds in isolated galaxies.
9. We argue that the evidence presented here supports a model where the absorption associated with group environments forms an intragroup medium in which one or more galaxies contribute material, and where galaxy interactions distribute the gas throughout the group halo. The gas may be dispersed by outflows from one galaxy entering the intragroup medium and eventually falling onto another group member galaxy (intergalactic transfer) and/or by tidal stripping from interactions that remove gas from one galaxy and place it in the intragroup medium.
10. Comparing our results to CIV and OVI in group envi-

ronments, we find that the low and higher ions behave differently compared to their respective isolated samples, presenting further evidence that these ions trace different components within the CGM and intragroup medium.

To better understand the gas traced by Mg II absorption, it would be helpful to examine the kinematics of the gas relative to the galaxy. While we have shown that absorbers associated with group galaxies have larger velocity dispersions, we do not yet know if the gas is being stripped from galaxies, accreting, or if the gas is truly associated with a single galaxy or not. We have statistically shown that the absorption is likely coupled to the group in an intragroup medium rather than individual galaxies, but the complexity of galaxy interactions may mean this is not always the case. More accurate galaxy redshifts and rotation curves, estimates of galaxy star formation rates, and deep surface brightness, high spatial resolution imaging of the galaxies in groups will improve the situation.

N.M.N. thanks John O’Meara for providing several reduced quasar spectra. This material is based on work supported by the National Science Foundation under grant No. 1210200 (NSF East Asia and Pacific Summer Institutes). N.M.N., G.G.K., and M.T.M. acknowledge the support of the Australian Research Council through a Discovery Project DP170103470. C.W.C. acknowledges support by the National Science Foundation under Grant No. AST-1517816. S.K.P. acknowledges support through the Australian Government Research Training Program Scholarship. M.T.M. thanks the Australian Research Council for Discovery Project grant DP130100568 which supported this work. Observations for the Q1038+064 were obtained with the Apache Point Observatory 3.5-meter telescope, which is owned and operated by the Astrophysical Research Consortium. Some of the data presented herein were obtained at the W. M. Keck Observatory, which is operated as a scientific partnership among the California Institute of Technology, the University of California and the National Aeronautics and Space Administration. The Observatory was made possible by the generous financial support of the W. M. Keck Foundation. Observations were supported by Swinburne Keck program 2017A_W248. The authors wish to recognize and acknowledge the very significant cultural role and reverence that the summit of Maunakea has always had within the indigenous Hawaiian community. We are most fortunate to have the opportunity to conduct observations from this mountain.

Facilities: Keck:II (ESI), APO (DIS)

REFERENCES

- Andrews, H., Barrientos, L. F., López, S., et al. 2013, *ApJ*, 774, 40
 Anglés-Alcázar, D., Faucher-Giguère, C.-A., Kereš, D., et al. 2017, *MNRAS*, 470, 4698
 Bergeron, J., & Boissé, P. 1991, *A&A*, 243, 344
 Bielby, R., Crighton, N. H. M., Fumagalli, M., et al. 2017, *MNRAS*, 468, 1373
 Bolzonella, M., Miralles, J.-M., & Pelló, R. 2000, *A&A*, 363, 476
 Bordoloi, R., Lilly, S. J., Kacprzak, G. G., & Churchill, C. W. 2014a, *ApJ*, 784, 108
 Bordoloi, R., Lilly, S. J., Knobel, C., et al. 2011, *ApJ*, 743, 10
 Bordoloi, R., Lilly, S. J., Hardmeier, E., et al. 2014b, *ApJ*, 794, 130
 Bouché, N., Hohensee, W., Vargas, R., et al. 2012, *MNRAS*, 426, 801
 Bouché, N., Murphy, M. T., Kacprzak, G. G., et al. 2013, *Science*, 341, 50
 Burchett, J. N., Tripp, T. M., Wang, Q. D., et al. 2018, *MNRAS*, 475, 2067
 Burchett, J. N., Tripp, T. M., Bordoloi, R., et al. 2016, *ApJ*, 832, 124
 Carswell, R. F., & Webb, J. K. 2014, VPFIT: Voigt profile fitting program, Astrophysics Source Code Library
 Chen, H.-W., Helsby, J. E., Gauthier, J.-R., et al. 2010, *ApJ*, 714, 1521
 Chen, H.-W., Lanzetta, K. M., Webb, J. K., & Barcons, X. 2001, *ApJ*, 559, 654
 Chen, H.-W., & Mulchaey, J. S. 2009, *ApJ*, 701, 1219
 Churchill, C. W. 1997, PhD thesis, University of California, Santa Cruz
 Churchill, C. W., Mellon, R. R., Charlton, J. C., et al. 2000, *ApJS*, 130, 91
 Churchill, C. W., Nielsen, N. M., Kacprzak, G. G., & Trujillo-Gomez, S. 2013a, *ApJ*, 763, L42
 Churchill, C. W., Trujillo-Gomez, S., Nielsen, N. M., & Kacprzak, G. G. 2013b, *ApJ*, 779, 87, (MAGIIICAT III)
 Churchill, C. W., Vander Vliet, J. R., Trujillo-Gomez, S., Kacprzak, G. G., & Klypin, A. 2015, *ApJ*, 802, 10
 Churchill, C. W., & Vogt, S. S. 2001, *AJ*, 122, 679
 Churchill, C. W., Vogt, S. S., & Charlton, J. C. 2003, *AJ*, 125, 98
 Chynoweth, K. M., Langston, G. I., Yun, M. S., et al. 2008, *AJ*, 135, 1983
 Coleman, G. D., Wu, C.-C., & Weedman, D. W. 1980, *ApJS*, 43, 393
 Danovich, M., Dekel, A., Hahn, O., Ceverino, D., & Primack, J. 2015, *MNRAS*, 449, 2087
 Danovich, M., Dekel, A., Hahn, O., & Teyssier, R. 2012, *MNRAS*, 422, 1732
 Dekker, H., D’Odorico, S., Kaufer, A., Delabre, B., & Kotzłowski, H. 2000, in *SPIE Conference Series*, Vol. 4008, *Optical and IR Telescope Instrumentation and Detectors*, ed. M. Iye & A. F. Moorwood, 534–545
 Evans, J. L. 2011, PhD thesis, New Mexico State University
 Ford, A. B., Davé, R., Oppenheimer, B. D., et al. 2014, *MNRAS*, 444, 1260
 Fraternali, F., van Moorsel, G., Sancisi, R., & Oosterloo, T. 2002, *AJ*, 123, 3124
 Gauthier, J.-R. 2013, *MNRAS*, 432, 1444
 Gehrels, N. 1986, *ApJ*, 303, 336
 Guillemin, P., & Bergeron, J. 1997, *A&A*, 328, 499
 Hani, M. H., Sparre, M., Ellison, S. L., Torrey, P., & Vogelsberger, M. 2018, *MNRAS*, 475, 1160
 Johnson, S. D., Chen, H.-W., & Mulchaey, J. S. 2013, *MNRAS*, 434, 1765
 Kacprzak, G. G., Churchill, C. W., Barton, E. J., & Cooke, J. 2011a, *ApJ*, 733, 105
 Kacprzak, G. G., Churchill, C. W., Ceverino, D., et al. 2010a, *ApJ*, 711, 533
 Kacprzak, G. G., Churchill, C. W., Evans, J. L., Murphy, M. T., & Steidel, C. C. 2011b, *MNRAS*, 416, 3118
 Kacprzak, G. G., Churchill, C. W., & Nielsen, N. M. 2012, *ApJ*, 760, L7
 Kacprzak, G. G., Churchill, C. W., Steidel, C. C., & Murphy, M. T. 2008, *AJ*, 135, 922
 Kacprzak, G. G., Murphy, M. T., & Churchill, C. W. 2010b, *MNRAS*, 406, 445
 Kacprzak, G. G., Vander Vliet, J. R., Nielsen, N. M., et al. 2018, *ApJ*, submitted
 Kacprzak, G. G., Martin, C. L., Bouché, N., et al. 2014, *ApJ*, 792, L12
 Kereš, D., Katz, N., Davé, R., Fardal, M., & Weinberg, D. H. 2009, *MNRAS*, 396, 2332
 Kottuš, S. M., Murphy, M. T., & Carswell, R. F. 2017, *MNRAS*, 464, 3679
 Lanzetta, K. M., & Bowen, D. 1990, *ApJ*, 357, 321
 Lilly, S. J., Carollo, C. M., Pipino, A., Renzini, A., & Peng, Y. 2013, *ApJ*, 772, 119
 Lopez, S., Barrientos, L. F., Lira, P., et al. 2008, *ApJ*, 679, 1144
 Martin, C. L., Shapley, A. E., Coil, A. L., et al. 2012, *ApJ*, 760, 127
 Meiring, J. D., Tripp, T. M., Prochaska, J. X., et al. 2011, *ApJ*, 732, 35
 Mihos, J. C., Keating, K. M., Holley-Bockelmann, K., Pisano, D. J., & Kassim, N. E. 2012, *ApJ*, 761, 186
 Murphy, M. 2016, UVES_popler: UVES_popler: P0st-PipeLine Echelle Reduction software, doi:10.5281/zenodo.56158
 Murphy, M. T., Kacprzak, G. G., Savorgnan, G. A. D., & Carswell, R. F. 2018, *MNRAS*, submitted
 Muzahid, S., Kacprzak, G. G., Churchill, C. W., et al. 2015, *ApJ*, 811, 132
 Nestor, D. B., Johnson, B. D., Wild, V., et al. 2011, *MNRAS*, 412, 1559
 Nestor, D. B., Turnshek, D. A., Rao, S. M., & Quider, A. M. 2007, *ApJ*, 658, 185
 Nielsen, N. M., Churchill, C. W., & Kacprzak, G. G. 2013a, *ApJ*, 776, 115, (MAGIIICAT II)
 Nielsen, N. M., Churchill, C. W., Kacprzak, G. G., & Murphy, M. T. 2013b, *ApJ*, 776, 114, (MAGIIICAT I)
 Nielsen, N. M., Churchill, C. W., Kacprzak, G. G., Murphy, M. T., & Evans, J. L. 2015, *ApJ*, 812, 83, (MAGIIICAT V)
 —. 2016, *ApJ*, 818, 171, (MAGIIICAT IV)
 Nielsen, N. M., Kacprzak, G. G., Muzahid, S., et al. 2017, *ApJ*, 834, 148
 Oppenheimer, B. D., & Davé, R. 2008, *MNRAS*, 387, 577
 Oppenheimer, B. D., Davé, R., Kereš, D., et al. 2010, *MNRAS*, 406, 2325
 Oppenheimer, B. D., Crain, R. A., Schaye, J., et al. 2016, *MNRAS*, 460, 2157

- Padilla, N., Lacerna, I., Lopez, S., et al. 2009, *MNRAS*, 395, 1135
- Peebles, M. S., Werk, J. K., Tumlinson, J., et al. 2014, *ApJ*, 786, 54
- Péroux, C., Rahmani, H., Quiret, S., et al. 2017, *MNRAS*, 464, 2053
- Petitjean, P., & Bergeron, J. 1990, *A&A*, 231, 309
- Pointon, S. K., Nielsen, N. M., Kacprzak, G. G., et al. 2017, *ApJ*, 844, 23
- Rahmani, H., Péroux, C., Augustin, R., et al. 2018, *MNRAS*, 474, 254
- Rubin, K. H. R., Prochaska, J. X., Koo, D. C., & Phillips, A. C. 2012, *ApJ*, 747, L26
- Rubin, K. H. R., Prochaska, J. X., Koo, D. C., et al. 2014, *ApJ*, 794, 156
- Rubin, K. H. R., Weiner, B. J., Koo, D. C., et al. 2010, *ApJ*, 719, 1503
- Rudie, G. C., Steidel, C. C., Trainor, R. F., et al. 2012, *ApJ*, 750, 67
- Sancisi, R., Fraternali, F., Oosterloo, T., & van der Hulst, T. 2008, *A&A Rev.*, 15, 189
- Schneider, D. P., Hartig, G. F., Jannuzi, B. T., et al. 1993, *ApJS*, 87, 45
- Schroetter, I., Bouché, N., Wendt, M., et al. 2016, *ApJ*, 833, 39
- Sheinis, A. I., Bolte, M., Epps, H. W., et al. 2002, *PASP*, 114, 851
- Steidel, C. C. 1995, in *QSO Absorption Lines*, ed. G. Meylan, 139
- Steidel, C. C., Dickinson, M., Meyer, D. M., Adelberger, K. L., & Sembach, K. R. 1997, *ApJ*, 480, 568
- Steidel, C. C., Dickinson, M., & Persson, S. E. 1994, *ApJ*, 437, L75
- Steidel, C. C., Kollmeier, J. A., Shapley, A. E., et al. 2002, *ApJ*, 570, 526
- Stern, J., Hennawi, J. F., Prochaska, J. X., & Werk, J. K. 2016, *ApJ*, 830, 87
- Stewart, K. R., Kaufmann, T., Bullock, J. S., et al. 2011, *ApJ*, 738, 39
- Thom, C., Werk, J. K., Tumlinson, J., et al. 2011, *ApJ*, 736, 1
- Tumlinson, J., Thom, C., Werk, J. K., et al. 2011, *Science*, 334, 948
- Werk, J. K., Prochaska, J. X., Thom, C., et al. 2012, *ApJS*, 198, 3
- . 2013, *ApJS*, 204, 17
- Werk, J. K., Prochaska, J. X., Cantalupo, S., et al. 2016, *ApJ*, 833, 54
- Whiting, M. T., Webster, R. L., & Francis, P. J. 2006, *MNRAS*, 368, 341
- Wolfe, S. A., Pisano, D. J., Lockman, F. J., McGaugh, S. S., & Shaya, E. J. 2013, *Nature*, 497, 224
- Wolynetz, M. S. 1979, *J. R. Stat. Soc.*, 28, 195

Table 1
Observed Galaxy Properties

(1)	(2)	Galaxy ID				B-band				K-band			
		(3)	(4)	(5)	(6)	(7)	(8)	(9)	(10)	(11)	(12)	(13)	(14)
QSO ^a	J-Name ^a	z_{gal}	$\Delta\alpha$ (arcsec)	$\Delta\delta$ (arcsec)	θ (arcsec)	Ref ^b	m_y^c	Band ^d	Ref ^b	m_y^e	Band ^d	Ref ^b	SED ^f
SDSS	J003340.21-005525.53	0.1760 0.1758	-8.2 18.9	7.2 2.7	10.91 19.09	6 6	20.98 21.01	g(AB) g(AB)	14 14	19.72 20.61	r(AB) r(AB)	14 14	E/S0 Im
SDSS	J005244.23-005721.7	0.13429 0.13465	-4.7 -3.1	12.6 35.4	13.42 35.55	10 10	16.84 19.52	r(AB) g(AB)	14 14	13.53 19.52	K_s (V) r(AB)	15 14	E/S0 Scd
		0.38260 0.38024	8.5 -0.3	-7.8 16.1	11.47 16.10	3, 19 ^b 19	21.15 22.81	F702W(V) F702W(V)	3 25	(Sbc) (Sbc)
0150-202^k	J015227.32-200107.10	0.38146 0.38140 0.38135	-7.8 -4.8 14.7	15.9 -27.3 -28.1	17.51 27.67 31.31	19 19 19	22.63 21.66 20.91	F702W(V) F702W(V) F702W(V)	25 25 25	(Sbc) (Sbc) (Sbc)
0151+045	J015427.99+044818.69	0.160 0.160	-6.2 -3.0	-1.7 10.5	6.40 10.90	1 1	19.10 20.20	$R_{\text{HROS}}(V)$ $R_{\text{HROS}}(V)$	1 1	(Sbc) (Sbc)
0226-4110 ^k	J022815.17-405714.3	0.2065 0.2078	-9.1 -24.9	-8.4 -25.9	10.87 32.04	21 21	21.94 20.29	R_J (AB) R_J (AB)	21 21	21.20 19.38	I_J (AB) I_J (AB)	21 21	E/S0 E/S0
0226-4110 ^k	J022815.17-405714.3	0.2678 0.2690 0.2680	16.9 8.5 36.2	-13.0 -36.7 -29.2	18.21 37.25 39.98	21 21 21	20.18 22.85 21.61	R_J (AB) R_J (AB) R_J (AB)	21 21 21	19.32 22.16 20.96	I_J (AB) I_J (AB) I_J (AB)	21 21 21	E/S0 E/S0 Sbc
0349-146 ^k	J035128.54-142908.71	0.324180 ^g 0.324651 ^g	13.0 -29.0	-23.5 18.5	26.72 34.44	22 22	20.00 19.50	F702W(AB) F702W(AB)	22 22	18.40 18.10	K_s (AB) K_s (AB)	22 22	E/S0 Sbc
0405-123	J040748.43-121136.65	0.16699 ^g 0.16699 ^g	-1.1 41.3	34.8 -1.8	34.81 40.36	22 22	21.04 17.43	R_J (AB) R_J (AB)	23 23	21.00 16.60	K_s (AB) K_s (AB)	22 22	Im Im
0450-131	J045313.48-130555.84	0.4941 0.4931	5.8 6.4	-5.9 -8.1	8.26 10.34	3 3	21.55 21.52	F702W(V) F702W(V)	3 3	17.64 17.64	K_s (V) K_s (V)	7 7	E/S0 E/S0
		0.2835 0.2821	11.6 12.6	-7.2 17.6	10.96 19.82	17 17	22.74 20.82	R_J (AB) R_J (AB)	17 17	(Sbc) (Sbc)
0515-4414	J051707.61-441056.2	0.2825 0.2823 0.2826	-25.2 32.2 -40.7	-8.5 -4.5 -7.7	19.93 23.52 30.16	17 17 17	19.07 18.73 18.72	R_J (AB) R_J (AB) R_J (AB)	17 17 17	(Sbc) (Sbc) (Sbc)
SDSS	J074528.15+191952.68	0.4582 0.4582	-15.0 -13.2	7.5 11.2	16.02 16.75	6 6	20.92 21.13	g(AB) g(AB)	14 14	19.81 20.33	r(AB) r(AB)	14 14	Scd Im
SDSS	J083220.74+043416.78	0.171224 ^g 0.1678 0.168222 ^g	12.9 -29.5 -32.7	-17.0 -30.2 -39.0	21.32 42.15 50.83	6 6 6	19.95 18.81 19.12	g(AB) g(AB) g(AB)	14 14 14	19.55 17.71 18.19	r(AB) r(AB) r(AB)	14 14 14	Im E/S0 Sbc

Table 1
(continued)

(1) QSO ^a	(2) J-Name ^a	(3) z_{gal}	Galaxy ID				B-band				K-band			
			(4) $\Delta\alpha$ (arcsec)	(5) $\Delta\delta$ (arcsec)	(6) θ	(7) Ref ^b	(8) m_r^c	(9) Band ^d	(10) Ref ^b	(11) m_r^c	(12) Band ^d	(13) Ref ^b	(14) SED ^f	
SDSS	J092554.71+400414.17	0.2475 0.2467	-8.0 -7.2	-20.8 -24.1	21.64 24.69	20 20	20.28 20.31	$g(\text{AB})$ $g(\text{AB})$	14 14	18.63 19.55	$r(\text{AB})$ $r(\text{AB})$	14 14	E/S0 Sbc	
SDSS	J092837.98+602521.02	0.1537 0.1542 0.1540	-3.5 30.2 67.2	-14.7 -12.1 -12.3	14.82 19.19 35.38	20 20 20	20.64 19.57 19.47	$g(\text{AB})$ $g(\text{AB})$ $g(\text{AB})$	14 14 14	20.05 18.99 18.40	$r(\text{AB})$ $r(\text{AB})$ $r(\text{AB})$	14 14 14	Scd Scd E/S0	
SDSS	J100902.06+071343.87	0.35585 ^g 0.35587 ^g	3.2 1.7	0.03 -9.3	3.13 9.41	20 20	24.10 21.65	F390W(AB) $g(\text{AB})$	24 14	23.21 20.96	F625W(AB) $r(\text{AB})$	24 14	Im Im	
1038+064	J104117.16+061016.92	0.306088 ^g 0.304858 ^g	14.1 10.7	15.4 25.5	20.70 27.61	2 2	18.48 20.87	F702W(V) F702W(V)	2 2	15.30 ...	$K_s(\text{V})$...	8 ...	E/S0 (Sbc)	
1127-145	J113007.05-144927.38	0.31207 ^g 0.3132 0.3124 0.31139 ^g	-3.9 9.3 7.8 21.7	0.5 3.8 16.0 -1.2	3.85 10.01 17.77 21.76	9 9 9 9	21.55 18.81 18.64 19.79	F814W(V) F814W(V) F814W(V) F814W(V)	9 9 9 9	...	$K_s(\text{V})$	(Sbc) E/S0 (Sbc) (Sbc)	
1127-145	J113007.05-144927.38	0.32839 0.32847	14.7 0.7	-6.9 19.3	16.23 19.29	3 3	20.19 18.89	F814W(V) F814W(V)	3 3	(Sbc) (Sbc)	
SDSS	J113327.78+032719.17	0.2367 0.2364	4.5 -4.1	-1.7 -9.6	4.79 10.39	20 20	19.84 20.16	$g(\text{AB})$ $g(\text{AB})$	14 14	18.62 19.01	$r(\text{AB})$ $r(\text{AB})$	14 14	E/S0 Sbc	
SDSS	J114830.12+021829.78	0.3206 0.3206	12.3 13.4	-21.9 -26.9	25.11 30.05	6 6	21.45 21.28	$g(\text{AB})$ $g(\text{AB})$	14 14	19.89 19.73	$r(\text{AB})$ $r(\text{AB})$	14 14	E/S0 E/S0	
SDSS	J121347.52+000129.99	0.2259 0.2258	-5.7 -6.4	6.6 11.3	8.72 12.99	6 6	20.59 21.06	$g(\text{AB})$ $g(\text{AB})$	14 14	19.20 20.29	$r(\text{AB})$ $r(\text{AB})$	14 14	E/S0 Scd	
SDSS	J132831.08+075942.01	0.2537 0.2549	1.0 -6.8	-18.1 23.2	18.13 24.16	6 6	21.74 20.38	$g(\text{AB})$ $g(\text{AB})$	14 14	20.47 19.06	$r(\text{AB})$ $r(\text{AB})$	14 14	E/S0 E/S0	
SDSS	J144033.82+044830.9	0.11271 0.11277	11.1 25.5	-5.8 19.5	12.49 32.05	10 10	18.17 16.79	$g(\text{AB})$ $g(\text{AB})$	14 14	18.17 16.79	$r(\text{AB})$ $r(\text{AB})$	14 14	Scd Sbc	
1556-245	J155941.40-244238.83	0.769 0.771	-3.0 -6.0	4.7 4.5	5.60 7.50	1 1	22.70 21.40	$R_{\text{EFOsc}}(\text{V})$ $R_{\text{EFOsc}}(\text{V})$	1 1	(Sbc) (Sbc)	
1622+238	J162439.08+234512.20	0.36809 ^g 0.368	-21.5 -24.1	-6.3 5.3	22.43 24.64	3 4	19.45 23.25	F702W(V) F702W(V)	3 3	15.90 19.52	$K_s(\text{V})$ $K_s(\text{V})$	4 4	E/S0 E/S0	

Table 1
(continued)

(1) QSO ^a	(2) J-Name ^a	(3) z_{gal}	Galaxy ID				B-band				K-band			
			(4) $\Delta\alpha$ (arcsec)	(5) $\Delta\delta$ (arcsec)	(6) θ (arcsec)	(7) Ref ^b	(8) m_{y}^{c}	(9) Band ^d	(10) Ref ^b	(11) m_{y}^{e}	(12) Band ^d	(13) Ref ^b	(14) SED ^f	
1623+269	J162548.79+264658.75	0.888 0.888	-1.0 -2.8	6.1 8.8	6.21 9.27	3 3	23.63 23.59	F702W(V) F702W(V)	3 3	18.30	K_s (V)	8	E/S0 (Sbc)	
SDSS	J204431.46+011312.43	0.1921 0.1927	6.1 -2.1	-3.6 -7.5	7.08 7.79	6 6	21.40 20.15	g (AB) g (AB)	14 14	20.66 18.93	r (AB) r (AB)	14 14	Sbc E/S0	
2126-158	J212912.17-153841.04	0.6668 0.6643 0.6647 0.6648	6.3 8.3 12.6 -14.5	-3.7 -3.2 -2.4 -19.4	7.10 8.60 12.40 23.90	16 16 16 16	20.79 20.34 22.08 20.88	i' (AB) i' (AB) i' (AB) i' (AB)	16 16 16 16	(Sbc) (Sbc) (Sbc) (Sbc)	
2128-123^k	J213135.26-120704.79	0.430200 ^g 0.43072 0.43006 0.42982	6.7 8.9 -17.2 -15.5	5.4 -5.9 -19.5 -26.4	8.63 10.52 25.76 30.45	3 18 18 18	20.43 25.73 ...	F702W(V) F702W(V) ...	3 25 ...	17.12	K_s (V)	7	E/S0 (Sbc) ...	

^a Groups included in the kinematics analysis are marked with bold-faced field names. We have the HIRES/Keck or UVES/VLT spectra for each bolded group, and have measurable M_{gII} above our detection threshold.

^b Galaxy Identification and Apparent Magnitude Reference: (1) Guillemin & Bergeron (1997), (2) this work, (3) Kacprzak et al. (2011b), (4) Steidel et al. (1997), (6) Chen et al. (2010), (7) Steidel et al. (1994), (8) Steidel (personal communication), (9) Kacprzak et al. (2010b), (10) Kacprzak et al. (2011a), (14) NED/SDSS, (15) NED/2MASS, (16) Whiting et al. (2006), (17) Bielby et al. (2017), (18) Péroux et al. (2017), (19) Rahmani et al. (2018), (20) Werk et al. (2012), (21) Chen & Mulchaey (2009), (22) Chen et al. (2001), (23) Johnson et al. (2013), (24) Meiring et al. (2011), and (25) this work.

^c Apparent magnitude used to obtain M_B .

^d Magnitude Band and Type: (AB) AB magnitude, and (V) Vega magnitude.

^e Apparent magnitude used to obtain M_K .

^f Galaxy Spectral Energy Distributions: (Sbc) No color information – Sbc used.

^g Redshift measured from Keck/ESI spectrum (this work).

^h The right ascension and declination for this galaxy reported by Rahmani et al. (2018) is incorrect.

^k Originally included as an isolated galaxy in MAGJICAT (Nielsen et al. 2013b).

Table 2
Calculated Galaxy and Absorption Properties

(1) QSO ^a	(2) J-Name ^a	(3) z_{gal}	Mg II Absorption					B-band				K-band		
			(4) z_{abs}	(5) $W_r(2796)$ Å	(6) DR	(7) Ref ^b	(8) D (kpc)	(9) K_{B_V} ^c	(10) M_B^d	(11) L_B/L_B^*	(12) K_{K_V} ^e	(13) M_K^d	(14) L_K/L_K^*	(15) $B-K$
SDSS	J003340.21-005525.53	0.1760 0.1758	0.1759	0.19 ± 0.04	...	6	32.3 56.4	0.40 0.02	-19.07 -18.66	0.23 0.16	0.31 -0.05	-21.26 -19.27	0.29 0.04	2.18 0.61
SDSS	J005244.23-005721.7	0.13429 0.13465	0.1346	1.46 ± 0.04	1.190 ± 0.05	10	31.7 84.3	-0.94 0.03	-21.22 -19.01	1.74 0.23	-0.26 0.05	-23.39 -19.99	2.14 0.09	2.16 0.97
		0.38260 0.38024					59.6 83.8	-1.02 -1.02	-19.49 -17.81	0.27 0.06
0150-202^k	J015227.32-200107.10	0.38146 0.38140 0.38135	0.383074	0.168 ± 0.015	1.17 ± 0.17	14	91.4 144.4 163.3	-1.02 -1.02 -1.02	-18.00 -18.97 -19.72	0.07 0.17 0.33
0151+045	J015427.99+044818.69	0.160 0.160	0.1602	1.55 ± 0.05	1.00 ± 0.09	1	17.5 29.8	-0.99 -0.99	-19.42 -18.32	0.32 0.12
0226-4110 ^k	J022815.17-405714.3	0.2065 0.2078	0.2067	< 0.02	...	5	33.6 108.9	-1.13 -1.13	-16.96 -18.63	0.03 0.15	0.52 0.52	-19.36 -21.19	0.05 0.27	2.40 2.56
0226-4110 ^k	J022815.17-405714.3	0.2678 0.2690 0.2680	0.2678	0.03 ± 0.01	...	5	62.8 153.6 164.4	-1.06 -1.06 -1.06	-19.43 -16.78 -18.01	0.29 0.02 0.08	0.56 0.56 0.56	-21.90 -20.08 -20.27	0.49 0.09 0.11	2.47 3.30 2.26
0349-146 ^k	J035128.54-142908.71	0.324180 ^g 0.324651 ^g	0.3244	< 0.015	...	14	125.5 161.9	-1.00 -0.70	-20.15 -20.95	0.52 1.09	-0.54 -0.55	-22.21 -22.50	0.63 0.82	2.02 1.55
0405-123	J040748.43-121136.65	0.16699 ^g 0.16699 ^g	0.167120	0.274 ± 0.002	1.26 ± 0.01	14	99.4 115.3	-0.44 -0.44	-18.04 -21.65	0.09 2.49	-0.36 -0.36	-18.16 -22.56	0.02 0.97	0.12 0.91
0450-131	J045313.48-130555.84	0.4941 0.4931	0.493936	0.674 ± 0.024	1.194 ± 0.059	3	49.7 62.2	-1.05 -1.05	-19.72 -19.74	0.29 0.30	-0.51 -0.51	-22.25 -22.24	0.59 0.59	2.53 2.50
		0.2835 0.2821					46.9 84.6	-0.71 -0.71	-17.36 -19.27	0.04 0.24
0515-4414	J051707.61-441056.2	0.2825 0.2823 0.2826	0.281772	0.733 ± 0.002	1.478 ± 0.007	14	85.1 100.4 128.8	-0.71 -0.71 -0.71	-21.02 -21.36 -21.37	1.23 1.67 1.69
SDSS	J074528.15+191952.68	0.4582 0.4582	0.4549	0.65 ± 0.1	...	6	92.6 96.8	0.73 0.38	-21.84 -21.29	2.13 1.28	0.25 -0.01	-23.04 -22.07	1.25 0.51	1.19 0.78
SDSS	J083220.74+043416.78	0.1678 0.168222 ^g	0.1684	0.20 ± 0.04	...	6	61.1 120.0 144.9	0.01 0.35 0.14	-19.62 -21.07 -20.56	0.38 1.46 0.91	-0.05 0.30 0.15	-20.25 -23.05 -22.32	0.11 1.53 0.78	0.63 1.97 1.76

Table 2
(continued)

(1) QSO ^a	(2) J-Name ^a	(3) z_{gal}	Mg II Absorption				B-band			K-band					
			(4) z_{abs}	(5) $W_{\lambda}(2796)$ Å	(6) DR	(7) Ref ^b	(8) D (kpc)	(9) K_{B^c}	(10) M_B^d	(11) L_B/L_B^*	(12) K_K^e	(13) M_K^d	(14) L_K/L_K^*	(15) $B-K$	
SDSS	J092554.71+400414.17	0.2475 0.2467	0.247604	1.18 ± 0.14	1.23 ± 0.22	14	84.0 95.6	0.76 0.36	-21.25 -20.52	1.57 0.80	1.37 1.06	-23.21 -21.98	1.67 0.54	1.96 1.46	
SDSS	J092837.98+602521.02	0.1537 0.1542 0.1540	0.153783	1.16 ± 0.16	1.10 ± 0.22	14	39.5 51.3 94.5	0.07 0.07 0.28	-18.76 -19.84 -20.14	0.18 0.48 0.63	0.47 0.47 1.23	-19.75 -20.81 -22.16	0.07 0.20 0.68	0.99 0.97 2.02	
SDSS	J100902.06+071343.87	0.35585 ^g 0.35587 ^g	0.355871	1.33 ± 0.17	1.25 ± 0.25	14	15.6 47.0	0.59 0.24	-17.87 -19.98	0.06 0.43	0.21 0.23	-18.39 -20.66	0.02 0.15	0.52 0.68	
1038+064	J104117.16+061016.92	0.306088 ^g 0.304858 ^g	0.3054	< 0.0419	...	14	92.8 123.3	-1.03 -1.06	-21.58 -19.15	1.99 0.21	-0.52 ...	-23.35 ...	1.82 ...	1.76 ...	
1127-145	J113007.05-144927.38	0.31207 ^g 0.3132 0.3124 0.31139 ^g	0.312709	1.769 ± 0.004	1.05 ± 0.09	13	17.3 45.6 80.8 98.8	-1.46 -1.89 -1.46 -1.46	-18.13 -20.45 -21.04 -19.88	0.08 0.70 1.20 0.41	...	-0.53 ...	-22.56 ...	0.87 ...	2.10 ...
1127-145	J113007.05-144927.38	0.32839 0.32847	0.328279	0.028 ± 0.003	1.560 ± 0.246	3	76.3 90.7	-1.46 -1.46	-19.62 -20.92	0.32 1.06	
SDSS	J113327.78+032719.17	0.2367 0.2364	0.237514	0.759 ± 0.005	1.456 ± 0.018	14	18.0 39.0	0.71 0.33	-21.24 -20.54	1.58 0.83	1.35 1.05	-23.10 -22.41	1.52 0.80	1.86 1.87	
SDSS	J114830.12+021829.78	0.3206 0.3206	0.3215	0.53 ± 0.02	...	6	116.2 139.1	1.11 1.11	-20.79 -20.96	0.94 1.10	0.55 0.55	-22.67 -22.81	0.96 1.10	1.88 1.85	
SDSS	J121347.52+000129.99	0.2259 0.2258	0.2258	0.54 ± 0.08	...	6	31.4 46.7	0.66 0.23	-20.32 -19.42	0.69 0.30	0.38 0.06	-22.41 -20.56	0.80 0.14	2.08 1.14	
SDSS	J132831.08+075942.01	0.2537 0.2537 0.2549	0.2545	0.79 ± 0.03	...	6	71.2 94.8 132.6	0.79 0.79 0.29	-19.59 -20.94 -20.64	0.34 1.17 0.89	0.42 0.42 0.07	-21.30 -22.76 -21.77	0.28 1.09 0.43	1.70 1.81 1.13	
SDSS	J144033.82+044830.9	0.11271 0.11277	0.11304	1.18 ± 0.04	1.280 ± 0.06	10	25.4 65.2	-0.01 0.00	-19.86 -20.98	0.51 1.43	0.05 0.12	-20.99 -22.69	0.24 1.16	1.12 1.71	
1556-245	J155941.40-244238.83	0.769 0.771	0.771483	2.49 ± 0.09	1.20 ± 0.07	14	41.2 55.2	-0.23 -0.23	-20.55 -21.86	0.46 1.53	
1622+238	J162439.08+234512.20	0.36809 ^g 0.368	0.368112	0.247 ± 0.005	1.248 ± 0.046	3	113.5 124.8	-1.29 -1.29	-20.81 -17.01	0.92 0.03	-0.53 -0.53	-23.21 -19.59	1.54 0.05	2.39 2.57	

Table 2
(continued)

(1) QSO ^a	(2) J-Name ^a	(3) z_{gal}	Mg II Absorption				B-band				K-band			
			(4) z_{abs}	(5) $W_r(2796)$ Å	(6) DR	(7) Ref ^b	(8) D (kpc)	(9) K_{By}^c	(10) M_B^d	(11) L_B/L_B^*	(12) K_{Ky}^e	(13) M_K^d	(14) L_K/L_K^*	(15) B-K
1623+269	J162548.79+264658.75	0.888 0.888	0.887679	0.903 ± 0.004	1.245 ± 0.01	3	47.9 71.4	0.12 -0.28	-20.36 -19.99	0.34 0.24	-0.64 ...	-23.01 ...	1.02 ...	2.65 ...
SDSS	J204431.46+011312.43	0.1921 0.1927	0.1927	0.50 ± 0.08	...	6	22.5 24.8	0.21 0.49	-18.67 -20.20	0.15 0.64	0.16 0.33	-19.98 -22.20	0.08 0.68	1.31 2.00
2126-158	J212912.17-153841.04	0.6668 0.6643 0.6647 0.6648	0.662742	1.903 ± 0.014	1.14 ± 0.02	14	49.7 60.1 86.7 167.2	-0.74 -0.74 -0.74 -0.74	-21.49 -21.93 -20.19 -21.39	1.22 1.82 0.37 1.11
2128-123^k	J213135.26-120704.79	0.43072 0.43006 0.42982	0.429735	0.395 ± 0.01	1.16 ± 0.05	3	48.1 59.1 144.5 170.8	-1.18 -0.99	-20.35 -15.25 -16.38 ^f -16.25 ^f	0.56 0.01 0.01 ^f 0.01 ^f	-0.51	-22.41	0.71	2.06

^a Groups included in the kinematics analysis are marked with bold-faced field names. We have the HIRES/Keck or UVES/VLT spectra for each bolded group, and have measurable Mg II above our detection threshold.

^b Mg II Absorption Measurements: (1) Guillemin & Bergeron (1997), (3) Kacprzak et al. (2011b), (6) Chen et al. (2010), (10) Kacprzak et al. (2011a), (13) Evans (2011), and (14) This work.

^c K-corrected used to obtain M_B from column (8) in Table 1 – Observed Galaxy Properties.

^d Absolute magnitudes are AB magnitudes.

^e K-corrected used to obtain M_K from column (11) in Table 1 – Observed Galaxy Properties.

^f R-band absolute magnitude, M_R , and luminosity, L_R/L_R^* , obtained from Péroux et al. (2017).

^g Redshift measured from Keck/ESI spectrum (this work).

^k Originally included as an isolated galaxy in MAGPICAT (Nielsen et al. 2013b).